



Insights into strain-induced solid mesophases in melt-spun polymer fibers

Edith Perret^{a,b,*}, Rudolf Hufenus^a

^a Laboratory for Advanced Fibers, Empa, Swiss Federal Laboratories for Materials Science and Technology, Lerchenfeldstrasse 5, 9014, St. Gallen, Switzerland

^b Center for X-ray Analytics, Empa, Swiss Federal Laboratories for Materials Science and Technology, Überlandstrasse 129, 8600, Dübendorf, Switzerland

ARTICLE INFO

Keywords:

Mesophase
Wide-angle x-ray diffraction
Melt-spun fibers
Quantification

ABSTRACT

This article provides an overview of strain-induced solid mesophases in polymer fibers, melt-spun from amorphous (polycarbonate, cyclo-olefin polymer, copolyamide, polyethylene terephthalate glycol) and semi-crystalline materials (polyethylene terephthalate, poly-3-hydroxybutyrate). The discussed mesophases are made of stretched, conformationally disordered macromolecules that are highly oriented along the fiber axis, and that reveal variations in their lateral spacing. Fitting algorithms for respective wide-angle x-ray diffraction (WAXD) patterns are put forward, and are directly tested on fibers melt-drawn from amorphous as well as semi-crystalline polymers. Equatorial, meridional, off-axis and azimuthal profiles are extracted from WAXD patterns and are simultaneously fitted. Best fit parameters contain detailed structural information, and lead to simulated 2D WAXD patterns, which in turn can be used to quantify the phases that are present in the fibers. We postulate that mesophases, which lead to broad equatorial reflections in WAXD patterns, can be found in all types of drawn melt-spun polymer fibers.

1. Introduction

Mesophases have been identified in many polymeric materials. The term ‘mesomorphic’ was first introduced by Friedel in 1922 [1], in order to describe an intermediate state of matter between liquid (or amorphous) and crystalline. In the literature, mesophases have been given many names: i) highly oriented non-crystalline mesophase (P_{nc}) [2–6], ii) intermediate phase [7–12], iii) oriented amorphous [13], iv) rigid and mobile amorphous [14–16], v) taut-tie non-crystalline phase [17], vi) paracrystalline phase [18], vii) solid mesophase [19] and viii) transient liquid crystalline mesophase [7,20–23], amongst others [24–34]. The reason why so many terms have been introduced, is that mesophases can have many different degrees of structural order. Therefore, classification is not always straight-forward. For example, terms i)–v) describe essentially the same state of matter, but the respective terminology emphasizes a specific property of the mesophase. In i), for example, the non-crystallinity (nonexistent unit cell) of the mesophase is emphasized, as well as the orientation of molecular chains. We have found this particular phase, P_{nc} , in many of the melt-spun polymer fibers that we are presenting in this article. This phase is made of highly oriented, aligned macromolecular chains, which reveal conformational disorder and variations in lateral spacing between the

chains. This mesophase leads to broad equatorial peaks or arcs in wide-angle x-ray diffraction (WAXD) patterns (Fig. 1). The term iii) describes that part of the amorphous phase becomes oriented. Since an amorphous phase is typically defined as having no long-range order and no orientation, we avoid to use this terminology in the remainder of this article and prefer to talk about a strain-induced highly oriented non-crystalline mesophase (P_{nc}) instead. The term vi), paracrystalline phase, does not describe the same phase as terms i)–v), in the sense that it states the existence of a unit cell. Paracrystalline phases are expected to show a broad equatorial peak and additional meridional, as well as off-axis reflections or streaks in the WAXD patterns [35]. Term vii), solid mesophase [19], has mainly been used as a collective term to describe the afore mentioned phases i)–vi). Term viii), liquid crystalline mesophase, describes a phase which combines the properties of a liquid (e.g. flow, ability to form droplets) and a crystalline solid (anisotropy in physical properties), and thus is not included in the collective term ‘solid mesophase’ [36]. In general, the molecules of liquid crystalline (LC) polymers are composed of rigid anisotropic mesogenic groups, which align along one direction. These mesogenic groups consist of at least two aromatic (or cycloaliphatic) rings, that are connected in the para positions by a rigid link, like for example in Kevlar. LC mesophases exhibit long-range orientational order, as crystals do, but without

* Corresponding author. Laboratory for Advanced Fibers, Empa, Swiss Federal Laboratories for Materials Science and Technology, Lerchenfeldstrasse 5, 9014, St. Gallen, Switzerland.

E-mail address: edith.perret@empa.ch (E. Perret).

<https://doi.org/10.1016/j.polymer.2021.124010>

Received 26 April 2021; Received in revised form 22 June 2021; Accepted 7 July 2021

Available online 9 July 2021

0032-3861/© 2021 The Authors. Published by Elsevier Ltd. This is an open access article under the CC BY license (<http://creativecommons.org/licenses/by/4.0/>).

three-dimensional positional order like it is the case in liquids [19,36,37]. WAXD patterns of LC mesophases show broad equatorial peaks and, in some cases, also meridional reflections (nematic, smectic) or azimuthally split meridional reflections [38]. Since LC phases give rise to very similar WAXD patterns as solid mesophases, the terms ‘smectic’ or ‘nematic’ have also often been used to describe the arrangement of high electron density groups in macromolecules, which do not contain mesogens [7,21,39] (see also Fig. 1).

A variety of WAXD patterns can typically be observed for melt-spun polymer fibers. Drawn melt-spun fibers show WAXD patterns with superimposed scattering features, which arise from different phases. For example, WAXD patterns of fibers, melt-drawn from amorphous polymers, show a superposition of the scattering from the amorphous phase (left panel, Fig. 1) with the scattering from a highly oriented mesophase P_{nc} (middle panel, Fig. 1). The amorphous phase is non-crystalline, has no long-range order and consists of not-oriented (spaghetti-like) macromolecules. The mesophase, however, consists of oriented chains, and the degree of the chain orientation influences the decay of the equatorial peak away from the equator. For unoriented chains, one observes ring-shaped isotropic scattering (amorphous), and for intermediate orientations, one observes an arc-shaped anisotropic equatorial scattering feature, where the equatorial position, $\mu^{P_{nc}}$, reflects the average lateral spacing between molecular chains, $d^{P_{nc}}$. For very high orientations, the mesophase gives rise to a pair of broad equatorial peaks in the WAXD pattern, which we could only observe in drawn semi-crystalline polymers. The 3D order of atomic positions, and the electron-density variations along the molecular chain (existence of heavy groups), determine whether additional meridional (or off-axis) reflections are observed (nematic, smectic). The nematic mesophase is made of highly oriented, yet conformationally disordered chains, where the atomic positions have no long-range order in the lateral direction. If the molecular chains contain heavy functional groups, arc-shaped meridional reflections can be observed, where the meridional positions, $\mu_{mer}^{P_{nc}}$, are linked to the vertical spacing between functional groups along the chain axis, $d_{mer}^{P_{nc}}$. In smectic mesophases, the chains arrange with their heavy groups aligned in planes perpendicular to the fiber axis without lateral order (smectic-A), or with additional pseudo-hexagonal lateral order (smectic-B). For these two phases, typically higher order meridional reflections are observed, and the differences between them are subtle. However, the meridional and equatorial reflections are sharper in the smectic-B phase, due to the higher order (larger correlation length) [40]. Note that other smectic phases (e.g. tilted structures) exist, which give rise to additional off-axis reflections (not shown in Fig. 1). For drawn fibers, melt-spun

from semi-crystalline polymers, the WAXD pattern is made of a superposition of three scattering features, arising from the amorphous phase, a highly oriented mesophase and the crystalline phase (right panel, Fig. 1). Mesophases in semi-crystalline polymers often consist of highly oriented and stretched tie molecules between crystals. The mesophases can, however, also develop from the amorphous phase through orientation and stretching of molecules.

In this article, we give an overview of different types of solid mesophases, which we have found in melt-spun polymer fibers produced at Empa (St. Gallen, Switzerland), or in commercially available fibers. It is well-known that spin-line stress, occurring in melt-spinning, can induce high orientation in polymeric fibers [41]. We have found mesophases in fibers melt-drawn from amorphous polymeric materials and from semi-crystalline polymers. In the literature, only a limited number of articles report solid mesophases in stretched non-crystalline polymer materials (cyclo-olefin polymer (COP) [42], copolyamide (coPA) [42], polystyrene (PS) [43–45] or poly(ester imide) [46]). In contrast, many mesophases have been reported to exist in semi-crystalline polymers, such as, polyethylene (PE) [26], polypropylene (PP) [26,34,47], isotactic propylene-1-butylene random copolymer [48], poly(1-butene) [26], poly(ethylene terephthalate) (PET) [2,3,8,10,12,13,18,32,43,49–55], poly(ethylene naphthalate) (PEN) [56], poly(ethylene furanate) (PEF) [57,58], polyamide 6 (PA6) or 6.6 (PA66) [39,59–61], polyamide 11 [62], poly(trimethylene terephthalate) [63], polylactic acid (PLA) [64–66], poly(L-lactic acid) (PLLA) [67–69] and copoly-sulfonamide (co-PSA) [70], amongst others.

In this article, we also present a 2D simulation and fitting method of WAXD patterns, which can be used to quantify mesophase, amorphous and crystalline phase in the fibers, respectively. The quantification of mesophases can be particularly useful to tailor mechanical properties, since mesophases have been shown to highly impact mechanical properties [8,41,71]. Only a few previous publications have suggested similar data treatment procedures to quantify mesophases [8,47,49,63,68,72–74]. Typically, authors have focused on quantifying the mesophase percentage in one particular sample. The ease of use and applicability of the fitting procedures, proposed in this article, are demonstrated for a variety of polymeric materials. The advantages of the proposed fitting procedures are that i) simulated 2D WAXD patterns are obtained, ii) the procedures work for amorphous as well as for semi-crystalline materials, iii) the underlying algorithm takes the unit cell crystal structure factor for semi-crystalline materials into account, iv) phases can be quantified, and v) detailed information about the mesophase scattering feature (e.g. location, sharpness, percentage and

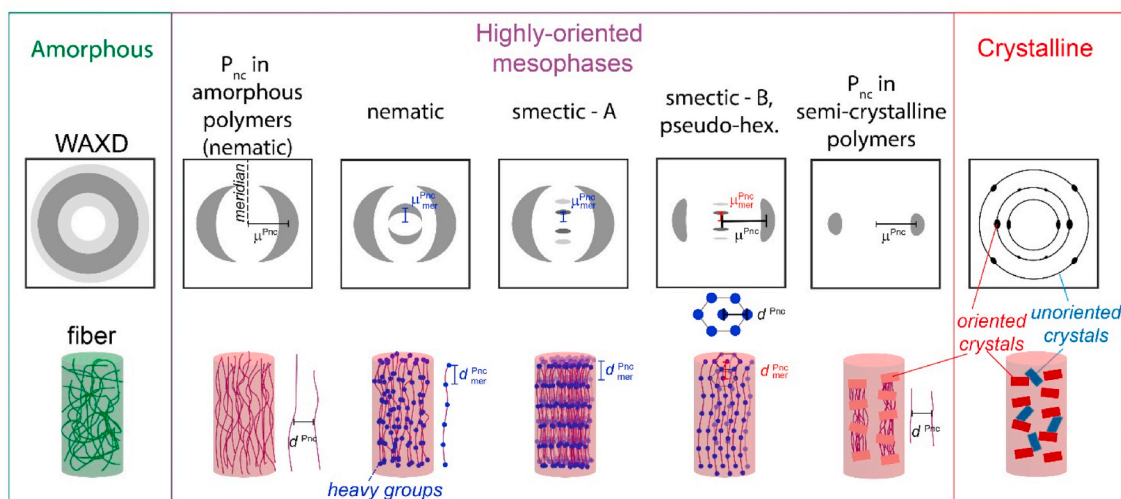


Fig. 1. Scattering features in WAXD patterns arising from an amorphous phase (left panel) or from a mesophase with highly oriented chains, where the atoms have different long-range order (middle panel) or from a crystalline phase (right panel).

orientation) can be simultaneously derived with details about both the crystalline phase (e.g. orientation, crystal size, amount of unoriented crystals) and the amorphous phase (e.g. preferred chain spacings).

2. Experimental section

2.1. Materials

A custom-made pilot-scale melt-spinning plant, described elsewhere [75], was used to produce monofilaments and bicomponent filaments from various materials. Details about melt-spinning parameters are given in the data in brief [76]. A PET monofilament (35 μm) has been obtained from Monosuisse AG (Emmen, Switzerland). The state of matter of raw material, raw material providers, fiber type, fineness, draw ratio (DR) and references to respective, previously published literature, are summarized in Table 1. The corresponding chemical structures of the polymer materials are summarized in Table 2.

2.1.1. Removal of PMP sheath from bicomponent fiber

The PMP sheath of the PETG/PMP bicomponent monofilament (Table 1) was dissolved in order to compare WAXD patterns from the PETG core with those of PETG monofilaments. Cut fiber pieces of the bicomponent filament were placed in a beaker filled with cyclohexane, which was stirred and maintained at a temperature of 45 °C. After 90 min, the fibers were taken out of the beaker, and washed with cyclohexane to remove any residues of PMP from the PETG core. The fiber samples have been subsequently dried in air.

2.2. WAXD and SAXS measurements

A Bruker Nanostar U diffractometer (Bruker AXS, Karlsruhe, Germany) was used to measure the WAXD and small-angle x-ray scattering (SAXS) patterns of melt-spun filaments or filament bundles. The Cu K α

2.3. WAXD fitting algorithms for drawn non-crystalline polymers

For the fitting of the 2D WAXD pattern of drawn non-crystalline polymer fibers, we have extracted azimuthal, equatorial and meridional profiles with the software DIFFRAC.EVA (version 4.2., Bruker AXS, Karlsruhe, Germany). Corresponding profiles, extracted from an air scattering pattern, are subtracted from these profiles, which are subsequently normalized to the maximum peak intensity in each profile. These normalized measured profiles were then simultaneously fitted with simulated profiles, using specifically developed Python codes. The Python package pyFAI [88] was used to extract profiles from simulated 2D WAXD patterns. The total mean square fitting error is given by the sum of fitting errors, χ_l^2 , of fitted profiles (Equation (1)),

$$\chi^2 = \sum_{l=1}^3 \chi_l^2 \quad (\text{Eq. 1})$$

$$\chi_l^2 = \frac{1}{N_l - n} \sum_{i=0}^{N_l-1} (I_{l,i}^{\text{meas}} - I_{l,i}^{\text{sim}})^2$$

with N_l being the number of simulated data points in profile l , and n the number of fitting parameters.

To properly fit the amorphous phase in the WAXD diffraction pattern, we had to add two or even three Gaussian rings on top of each other, one with a broad width, which reflects the random distances between unoriented chains, and one or two rings with a narrower width, which describe preferred distances between unoriented chains. It was also necessary to introduce a factor, k , to slightly distort the amorphous ring to an elliptic trace, since for highly drawn samples, the chains aligned along the fiber axis tend to be closer together than for the chains aligned perpendicular to the fiber axis ($k > 1$). Equation (2) gives an example of the superposition of two Gaussian rings.

$$I_{\text{amorphous}} = A \exp \left[-\frac{(\sqrt{2\theta x^2 + k2\theta y^2} - \mu_1)^2}{2\sigma_1^2} \right] P + B \exp \left[-\frac{(\sqrt{2\theta x^2 + k2\theta y^2} - \mu_2)^2}{2\sigma_2^2} \right] P \quad (\text{Eq. 2})$$

radiation ($\lambda = 1.5419 \text{ \AA}$) was sent through a beam defining pinhole of 300 μm to the filaments, and the diffraction pattern was recorded with a VÅNTEC-2000 MikroGap area detector (Bruker AXS, Karlsruhe, Germany). The distance of the sample to the active detector area was typically close to 9.2 cm, and the exposure times were either 1800 s or 3600 s for WAXD. The measured intensities of WAXD patterns have been divided by the fiber cross-sectional area, in order to account for the thinning of the fibers due to drawing. WAXD measurements were per-

Here, P is the polarization factor, which has already been explained elsewhere [85]. The seven or ten fitting parameters, depending on the amount of rings used, were: the height of the Gaussian peaks, A , B , C ; the positions, μ_1 , μ_2 , μ_3 ; the widths, σ_1 , σ_2 , σ_3 ; the factor k , to render an elliptic trace. To simulate the mesophase, we have used a damped asymmetric Gaussian function (Equation (3)).

$$I_{\text{eq}}^{\text{Pnc}} = D \exp \left[-\frac{(2\theta - \mu_{\text{Pnc}})^2}{2\sigma_{\text{Pnc}}^2} \right] \left(1 + \text{erf} \left\{ \frac{a(2\theta - \mu_{\text{Pnc}})}{\sigma_{\text{Pnc}} \sqrt{2}} \right\} \right) \exp \left[-\frac{4\pi^2}{3} (s_3^2 \Delta X_{\text{Pnc}}^2) \right] P \quad (\text{Eq. 3})$$

formed in order to quantify the mesophase content and obtain structural information. SAXS measurements were performed to verify if lamellae are present in the fibers. For SAXS, the sample to active detector area distance was typically close to 110.5 cm, and exposure times were 4600s. A significant scattering signal was observed for hardly any SAXS patterns, thus they are only shown in the data in brief [76].

The fitting results of several polymer fibers prove that this chosen fitting function for the mesophase represents the data very well. Here, the five fitting parameters were: the height of the mesophase, D ; its position, μ_{Pnc} ; its width, σ_{Pnc} ; the asymmetry factor a ; the damping factor ΔX_{Pnc} . For a fully isotropic sample, ΔX_{Pnc} would be equal to zero.

In case of coPA, a meridional reflection was observed, which is dis-

Table 1

Summary of studied polymer materials and produced fibers thereof [77,78,80,84].

State of matter of raw material	Raw material	Raw material providers	Fiber type	Diameter ^a [μm]	Fineness [tex= mg/m]	DR
amorphous	Polycarbonate (PC)	Lexan 103R	Monofilaments	168	26.7	1.0
		Sabic, Bergen op Zoom, The Netherlands [77]		117	13.0	2.0
				98	9.1	3.0
	Cyclo-olefin polymer (COP)	Zeonor 1020 R	Monofilaments [42, 79]	133	14.0	1.5
		Zeon Europe GmbH, Düsseldorf, Germany [78]		126	12.5	2.0
				109	9.4	2.5
				91	6.5	3.0
	Copolyamide (coPA)	Grilamid® TR 90	Monofilaments [42]	70	3.8	2.5
		EMS Chemie AG, Domat-Ems, Switzerland [80]		79	4.9	3.0
	Polyethylene terephthalate glycol (PETG)	Eastar CoPES 6763, Eastman Chemical Company, Anniston AL, USA [81]	As-spun PETG monofilament	184	33.6	1.0
Bicomponent core/sheath monofilament (PETG/PMP)			d _{core} =106 μm d _{fiber} =183 μm			
semi-crystalline	Polymethyl-pentene (PMP or TPX)	TPX™ Mitsui Chemicals, Tokyo, Japan [82]	PMP monofilament	140	12.8	9.6
	Polyethylene terephthalate (PET)	Grisuten, Märkische Faser GmbH, Premnitz, Germany	Monofilaments	35	1.4	5.2
	Poly-3-hydroxybutyrate (P3HB)	Biomer, Krailling, Germany	Monofilament No. 1108 (II) [4, 5, 83-85]	90	7.5	6.0

^a Calculated from the linear mass density of the fiber and the density of the polymer: $\rho_{COP} = 1.01 \text{ g/cm}^3$, $\rho_{PC} = 1.20 \text{ g/cm}^3$, $\rho_{coPA} = 1.00 \text{ g/cm}^3$, $\rho_{coPA} = 0.83 \text{ g/cm}^3$.

Table 2
Chemical structures of analyzed polymer materials.

State of matter of raw material	Raw material	Chemical structures
amorphous	Polycarbonate (PC) [86]	
	Cyclo-olefin polymer (COP) [42,79]	
	Co-polyamide (coPA) (Grilamid® TR90 from EMS Chemie AG, Domat-Ems, Switzerland) [42,87]	
	Polyethylene terephthalate glycol (PETG) [81]	
Semi-crystalline	Polymethyl-pentene (PMP or TPX) [82]	
	Polyethylene terephthalate (PET)	
	Poly-3-hydroxybutyrate (P3HB)	

cussed in more detail in the results section. The meridional reflection was simulated with an additional damped Gaussian function (Equation (4)) and was added to the mesophase intensity.

$$I_{mer}^{Pnc} = E \exp\left[-\frac{(2\theta - \mu_{mer})^2}{2\sigma_{mer}^2}\right] \exp\left[-\frac{4\pi^2}{3} (s_{12}^2 \Delta X_{mer}^2)\right] P \quad (\text{Eq. 4})$$

Further details about the used fitting parameters for the individual melt-spun fibers are given in the data in brief [76].

2.4. WAXD fitting algorithms for drawn semi-crystalline polymers

The simulations of the crystalline phase in 2D WAXD patterns are based on the theory by Burger et al. [89]. This theory has already been successfully applied to a variety of semi-crystalline polymers by other authors and us [48,90–92].

In order to calculate the intensity of Bragg reflections of individual (*hkl*) planes, it is necessary to know the atomic positions of all atoms in the unit cell, since the scattered intensity of an (*hkl*) plane is directly proportional to the modulus square of the unit cell structure factor, $|F_{hkl}(s_{hkl})|^2$ (Equation (5)).

$$|F_{hkl}(s_{hkl})|^2 = \left| \sum_{j=1}^N f_j \exp(-2\pi i(s_{hkl} \cdot \mathbf{R}_j)) \exp\left(-B \frac{|s_{hkl}|^2}{4}\right) \right|^2 \quad (\text{Eq. 5})$$

The scattering vectors, s_{hkl} , of (*hkl*) planes represent the nodes in reciprocal space, with $|s_{hkl}| = 2\sin(\Theta_{hkl})/\lambda$. The atomic form factors, f_j , are calculated using the coefficients from the international tables for crystallography [93,94]. Isotropic thermal displacement parameters, B , for the Debye-Waller factor calculations, as well as unique atomic positions, unit cell lattice parameters and space groups, are taken from published articles [95–97]. Applying the correct symmetry operations

leads to the thought-after atomic coordinates x_j, y_j, z_j of all atoms in the unit cell, from which the atomic position vectors, \mathbf{R}_j , can be calculated [92].

The measured WAXD intensity is proportional to the averaged intensity from the (hkl) planes over the spherical surface with radius $|s_{hkl}|$. The finite crystallite size, W , leads to a fixed width, $w = 1/W$, of the reflections in reciprocal space. Since the crystal size depends on the chosen crystalline direction, which is perpendicular to the crystal planes of the chosen reflection, different width parameters have been introduced for equatorial reflections. We make use of a Lorentzian distribution function to account for the broadening of the peaks due to the finite crystal size. The scattered intensity distribution of a (hkl) plane with polar angle ϕ_{hkl} is given by Equation (6).

$$\overline{I(s, \phi_{hkl})} = \frac{1}{\left(4\pi w |s_{hkl}|^2\right)} I_{hkl}(s_{hkl}) \frac{1}{1 + [\pi(s - s_{hkl})/w]^2} \quad (\text{Eq. 6})$$

The scattered intensity $I_{hkl}(s_{hkl})$, is proportional to the above given unit cell structure factors squared. The Onsager distribution function, $F(\phi, \phi_{hkl})$, takes the orientation of the crystallites into account, where p_0 is the isotropic randomly oriented fraction of crystals in the filament, p is the azimuthal width of the peaks, arising from the oriented crystal fraction, and I_0 is the modified Bessel function of the first kind of order zero (Equation (7)).

$$F(\phi, \phi_{hkl}) = p_0 + (1 - p_0) \left(\frac{p \cosh(p \cos \phi \cos \phi_{hkl})}{\sinh(p)} \right) I_0(p \sin \phi \sin \phi_{hkl}) \quad (\text{Eq. 7})$$

Reflections with large $|s_{hkl}|$ are typically attenuated in measured 2D WAXD patterns, which can be explained by crystal imperfections, where atomic groups are displaced statistically around their ideal position [92]. Thus, a Debye-Waller factor, DWF , is applied to correct the intensity for this disorder.

The overall averaged intensity arising from the crystals in the filament is given by Equation (8).

$$\overline{J(s, \phi)} = \overline{I(s, \phi_{hkl})} F(\phi, \phi_{hkl}) DWF \quad (\text{Eq. 8})$$

Typically, one or two Gaussian rings, $I_{\text{amorphous}}$, were used to simulate the intensity contribution from the unoriented, amorphous phase (Equation (2)), and a damped asymmetric Gaussian profile, I_{Pnc} (Equation (3)), was used to simulate the equatorial intensity contribution from a highly oriented non-crystalline mesophase, P_{nc} . Finally, the overall intensity distribution of the simulated 2D WAXD pattern is described by Equation (9).

$$I_{\text{sim}}(s, \phi_{hkl}) = I_{\text{amorphous}} + I_{\text{Pnc}} + \overline{I(s, \phi_{hkl})} F(\phi, \phi_{hkl}) DWF \quad (\text{Eq. 9})$$

Background corrected, normalized integrated azimuthal, equatorial as well as off-axis profiles were simultaneously fitted with simulated profiles by minimizing the total fitting error, χ^2 , using a differential evolution method (Eq. (1)). To calculate the fitting errors, the measured profiles were interpolated to the simulated angular data points. Details about the used fitting parameters for PET and P3HB filaments are given in the data in brief [76].

2.5. Calculation of phase percentages

The phase percentages have been calculated by dividing the sum of the entire 2D map intensity contribution of the phase of interest by the total simulated scattered intensity. Equation (10) shows how the intensity contribution from the mesophase is calculated.

$$\chi_{\text{Pnc}}(\%) = \frac{I_{\text{Pnc}}}{I_{\text{amorphous}} + I_{\text{Pnc}} + I_{\text{cryst}}} \times 100 \quad (\text{Eq. 10})$$

3. Results and discussion

3.1. Drawn fibers melt-spun from amorphous polymers

3.1.1. Uniqueness of fitting solution and algorithm

As described in the experimental section, 2D WAXD patterns are simulated using several 2D functions (one asymmetric Gaussian for the mesophase and several Gaussian rings for the amorphous phase), followed by an extraction of equatorial, meridional and azimuthal profiles, which are subsequently fitted to the extracted, measured profiles. The fact that these different profiles (azimuthal, equatorial and meridional) are fitted simultaneously, limits the number of possible solutions that can be found, since each profile gives characteristic information about specific phases. Even though the scattering signal of the amorphous phase and mesophase overlap, the simultaneous fitting of the three profiles ensures that the phases become deconvolved. For example, the azimuthal profile can either be flat, which signifies that no mesophase is present, or it shows a mesophase peak on the equator. Thus, the fit of the azimuthal profile mainly optimizes the decay (orientation) parameter of the mesophase, and both intensities of mesophase and amorphous phase. However, the meridional profile is mainly sensitive to the amorphous phase contribution (unoriented fraction), and the equatorial profile is sensitive to both amorphous and mesophase position/width/asymmetry/intensity parameters. We have ensured that only the minimum amount of Gaussian rings has been used to fit the amorphous phase contribution, in order to properly fit the profiles. Using less than 3 or 2 Gaussian rings, depending on the sample, significantly increased the fitting error, and especially the meridional profile could not be well reproduced. Other solutions with local minimum errors may exist, depending on the chosen initial parameters, but it is expected that the solutions would contain similar peak positions and widths.

Other authors have used 'the halo method' [47,63] to extract the isotropic fraction (amorphous phase) from WAXD patterns. In this method, the minimum intensity values in azimuthal scans yield the profile from the amorphous phase contribution, as a function of scattering angle 2θ . However, this method becomes problematic when, e.g., the mesophase decay is very shallow and still gives rise to contributions at the meridian, as it is the case in the following fitting examples. Fitting WAXD patterns, while enforcing that the mesophase does not contribute to the meridional profile, led to significantly larger errors in the azimuthal profiles. Note that the mesophase, which is described in the following sections, is the orientable fraction of the material.

3.1.2. WAXD fitting results

In the next sections, we are discussing the structural details of mesophases and amorphous phases that we have found in monofilaments melt-spun from amorphous polymers (PC, COP, coPA), and in the PETG core of a bicomponent PETG/PMP fiber. Even though these are all amorphous polymers, their molecular chains can be oriented and stretched through drawing, leading to a highly oriented mesophase. For all drawn PC, COP and coPA monofilaments, we have found nematic mesophases, and the quantification of mesophase and amorphous phase has been successfully performed through a 2D WAXD fitting method.

3.1.2.1. Polycarbonate monofilaments. We have measured WAXD patterns of three melt-spun PC fibers of different draw ratios. The top row in Fig. 2 shows the measured WAXD patterns, where the intensities have been divided by the fiber cross-sectional area, in order to account for the

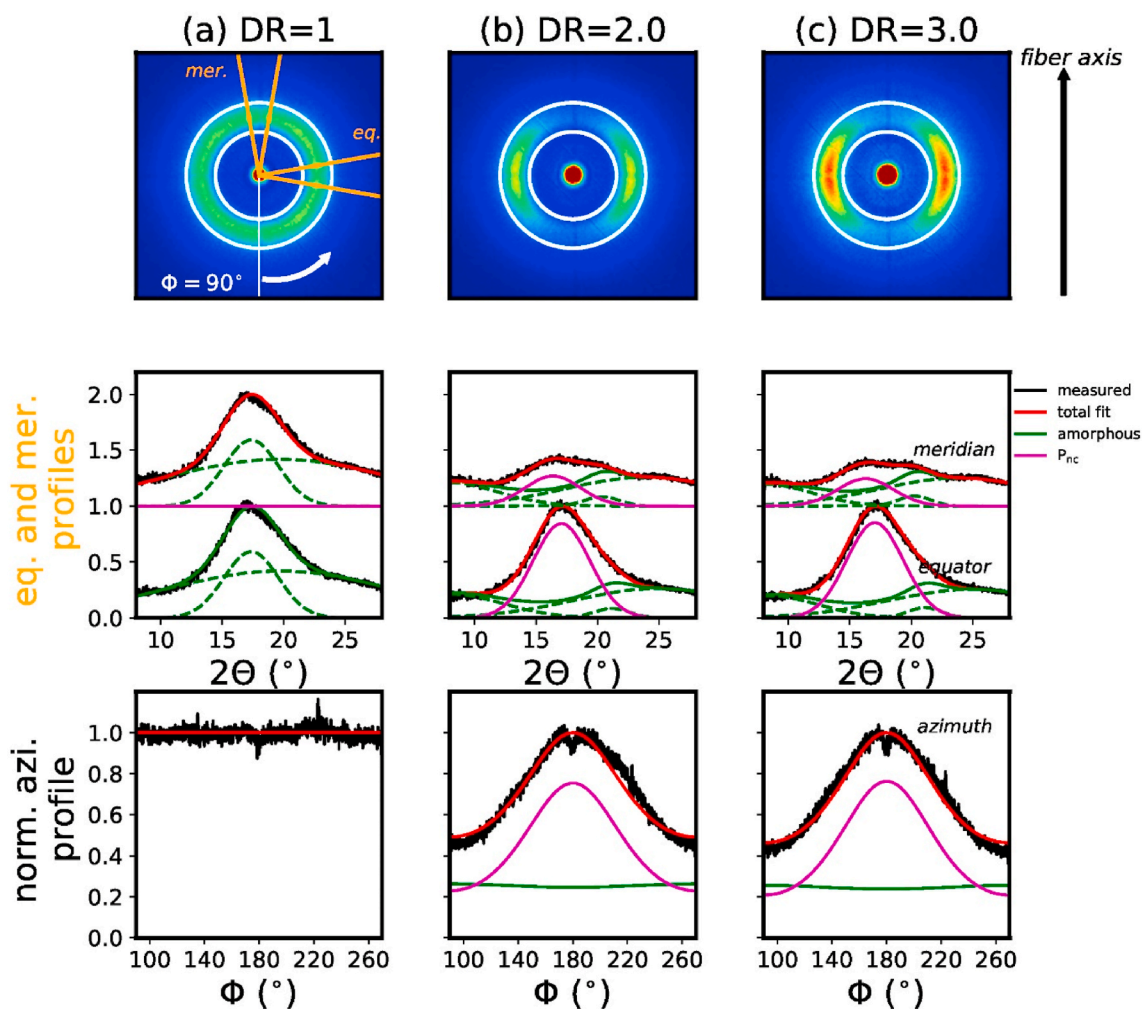


Fig. 2. Measured WAXD patterns of PC fibers (top row) with corresponding fits of equatorial (eq.) and meridional (mer.) (middle row), as well as azimuthal profiles (bottom row). The equatorial and meridional profiles are shown normalized to the maximum equatorial intensity, and the azimuthal profiles to the maximum azimuthal intensity. The meridional profiles are offset by +1 for better visibility.

thinning of the fibers due to drawing. The integrated meridional (mer.) and equatorial (eq.) sectors (opening angle 20°) are highlighted with orange lines, and the integrated azimuthal ring is indicated with white circles. The middle row in Fig. 2 shows both, equatorial and meridional profiles, and the bottom row displays the azimuthal profiles.

As expected, the as-spun fiber, wound-up directly after spinning without drawing (DR = 1), is completely amorphous, as indicated by the completely flat azimuthal profile arising from the amorphous Gaussian ring in the 2D pattern (Fig. 2a). Upon drawing, two arc-shaped equatorial reflections appear in the WAXD pattern, which arise from the P_{nc} mesophase (Fig. 1), where PC chains are stretched along the fiber axis and have a preferred lateral spacing. 2D WAXD patterns have been simulated from best fit parameters and are shown in Fig. 3 (2nd row). The simulated WAXD pattern can be split into two contributions, one arising from the amorphous phase (3rd row), and one from the highly oriented non-crystalline mesophase (4th row). The best fit parameters and calculated phase percentages are given in Table 4.

Interestingly, the amorphous phase (3rd row in Fig. 3) for filament DR 1 consists of a superposition of two rings, a sharp and a broad ring. We suspect that the very broad halo arises from intramolecular

interferences (within chains) between heavier atoms, and that the inner sharper halo arises from intermolecular interferences (between chains), reflecting the distances between macromolecules. The good fit of the WAXD data of this PC filament with DR 1, proves that the Gaussian functions for the amorphous phase are well representing the scattering of the unoriented amorphous phase. For the drawn filaments, DR 2 and DR 3, it is necessary to introduce three rings to fully describe the amorphous pattern in the background, since part of the intensity is redistributed into the mesophase scattering feature. Additionally, the rings become elliptically shaped upon drawing, which can also be seen by the increase in the k parameter in Table 4. The overall percentage of the mesophase, $\chi_{P_{nc}}$, is significantly increasing from DR 1 to DR 2, at the expense of the amorphous phase. Between DR 2 and DR 3, however, the mesophase percentage stays almost constant, since not only the mesophase scattering becomes more intense upon drawing, but also the overall scattering signal. This suggests that the electron density contrast in the material increases upon drawing, which could arise from the formation of small voids. However, the SAXS pattern shows no significant scattering feature for DR 3 [76].

The position of the sharp amorphous ring, μ_1 (Table 5), in the as-spun

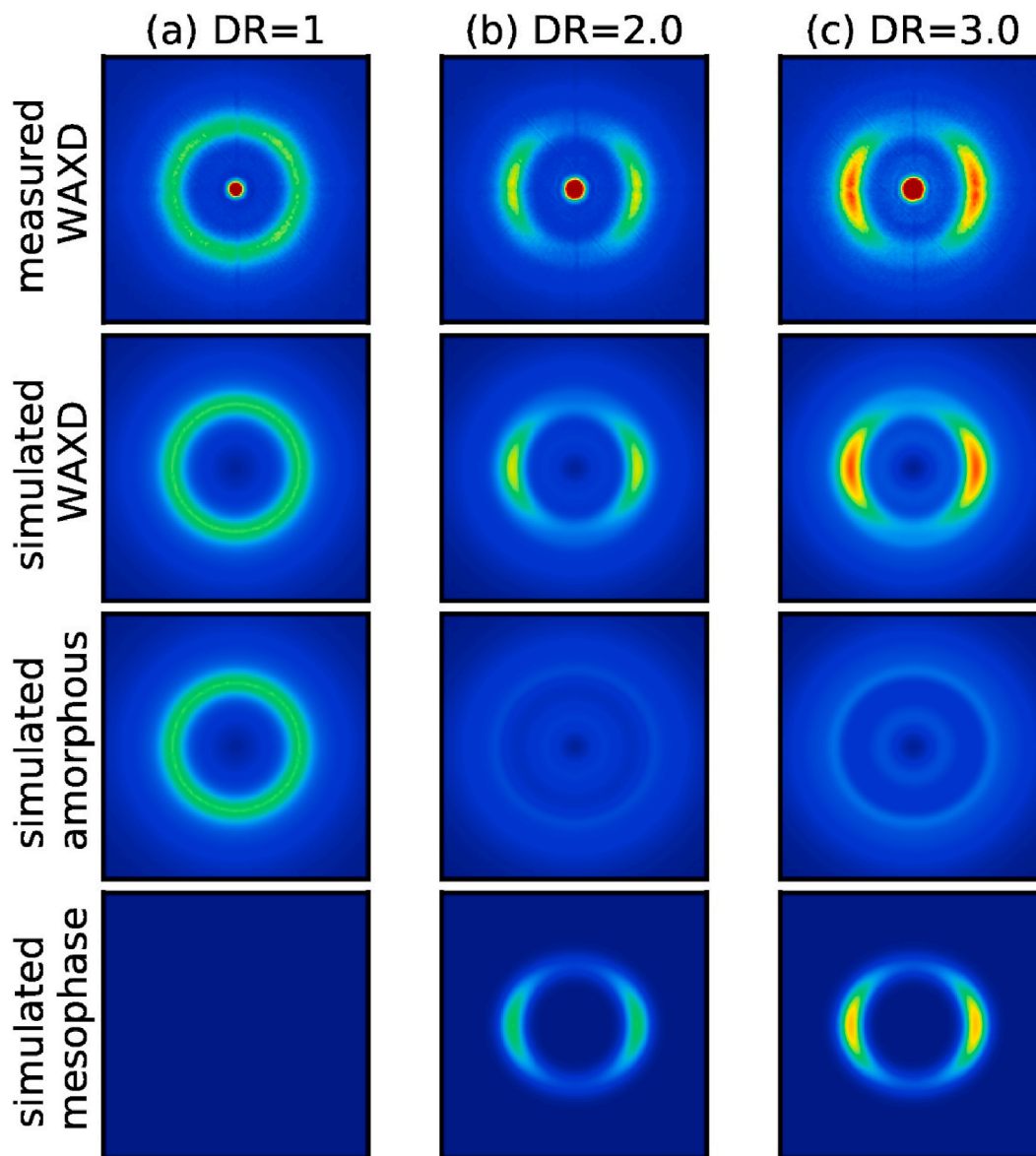


Fig. 3. Measured WAXD patterns of PC fibers for different draw ratios (1st row), simulated WAXD patterns resulting from the best fits (2nd row), simulated amorphous phase (3rd row) and simulated mesophase (4th row).

fiber (DR 1) is almost at the same angle as the mesophase, which develops upon drawing. This suggests that a preferred distance, ~ 5.1 Å, exists between unoriented chains in the amorphous phase of the as-spun fiber, and that these chains orient upon drawing, while maintaining their distance.

3.1.2.2. Cyclo-olefin polymer monofilaments. The chemical structure of COP consists of bulky ring moieties in the chain (Table 2), causing this material to be amorphous in nature. Profiles of WAXD patterns of four differently drawn COP fibers (DR = 1.5, 2.0, 2.5, 3.5) have been fitted [76]. The measured and simulated WAXD patterns are shown in Fig. 4. Here, the WAXD pattern of the amorphous phase (3rd row) consists of a superposition of only two rings. Analogously to the PC fibers, one ring has a rather small width, whereas the second one is broad. The 4th row in Fig. 4 shows the mesophase contribution.

The overall percentage of the mesophase, χ_{pnc} , is increasing between DR 1.5 and DR 2.0, on the expense of the amorphous phase (Table 4). For higher draw ratios, the mesophase percentage stays almost constant, even though it shows a significant sharpening on the equator, which is reflected by the increase in the peak intensity, D_{norm} , and the azimuthal decay parameter, ΔX_{pnc} (see also azimuthal profiles in data in brief [76]). The increase in the decay parameter correlates with an increase in the molecular orientation parameter from $f_{\text{pnc}} = 0.44$ to $f_{\text{pnc}} = 0.50$ for draw ratios 1.5 to 3.0. This Hermans' orientation parameter [98], f_{pnc} , can be calculated from the azimuthal profile of the mesophase [76]. The fact that the overall percentage of the mesophase is not changing much above DR 2.0, suggests that only a fixed amount of chains are flexible enough to stretch and orient along the fiber axis, while being laterally squeezed. The latter is also reflected by an increase in the angular position of the mesophase peak, $\mu_{\text{pnc}}^{\text{max}}$, on the equator, which correlates with

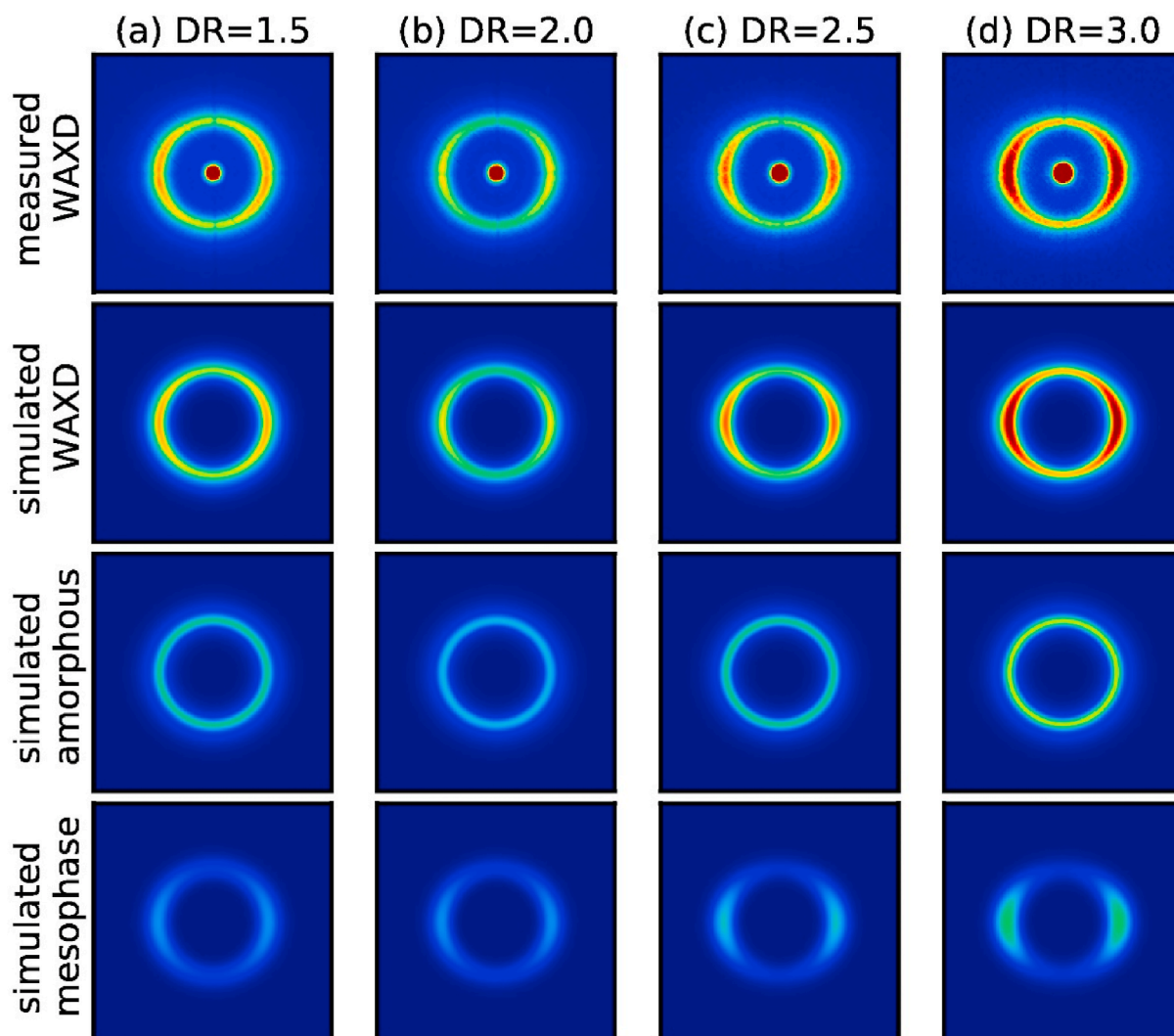


Fig. 4. Measured WAXD patterns of COP fibers for different draw ratios (1st row), simulated WAXD patterns resulting from the fits (2nd row), simulated amorphous phase (3rd row) and simulated mesophase (4th row).

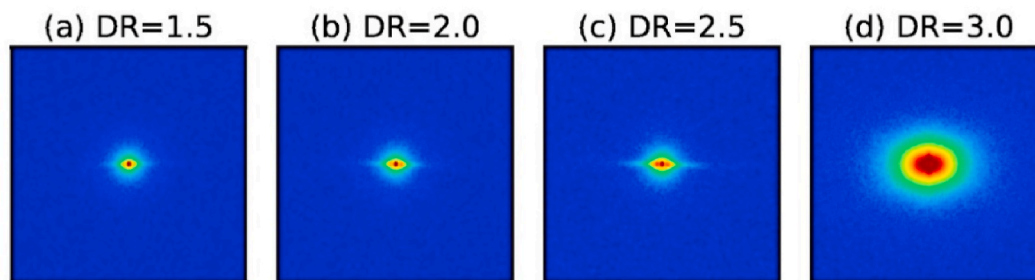


Fig. 5. Measured SAXS patterns of COP fibers.

a decrease in the lateral spacing, d_{PNC} , between chains in the mesophase (Table 5).

Fig. 5 shows the measured SAXS patterns (angular range -2 to 2°) of all COP fibers. The central diffuse scattering is significantly stronger for the highly drawn fiber, DR 3.0. This scattering is most-likely arising from low-density structures like microvoids or cracks in the fiber. This

assumption explains the increase in the electron density contrast and thus overall scattering with increasing draw ratio.

3.1.2.3. Co-polyamide monofilaments. The coPA Grilamid® TR90 is a copolymer of dodecanedioic acid and 4,4'-methylenabis(2-methyl-cyclohexanamine) (Table 2). Fig. 6 shows the measured and simulated

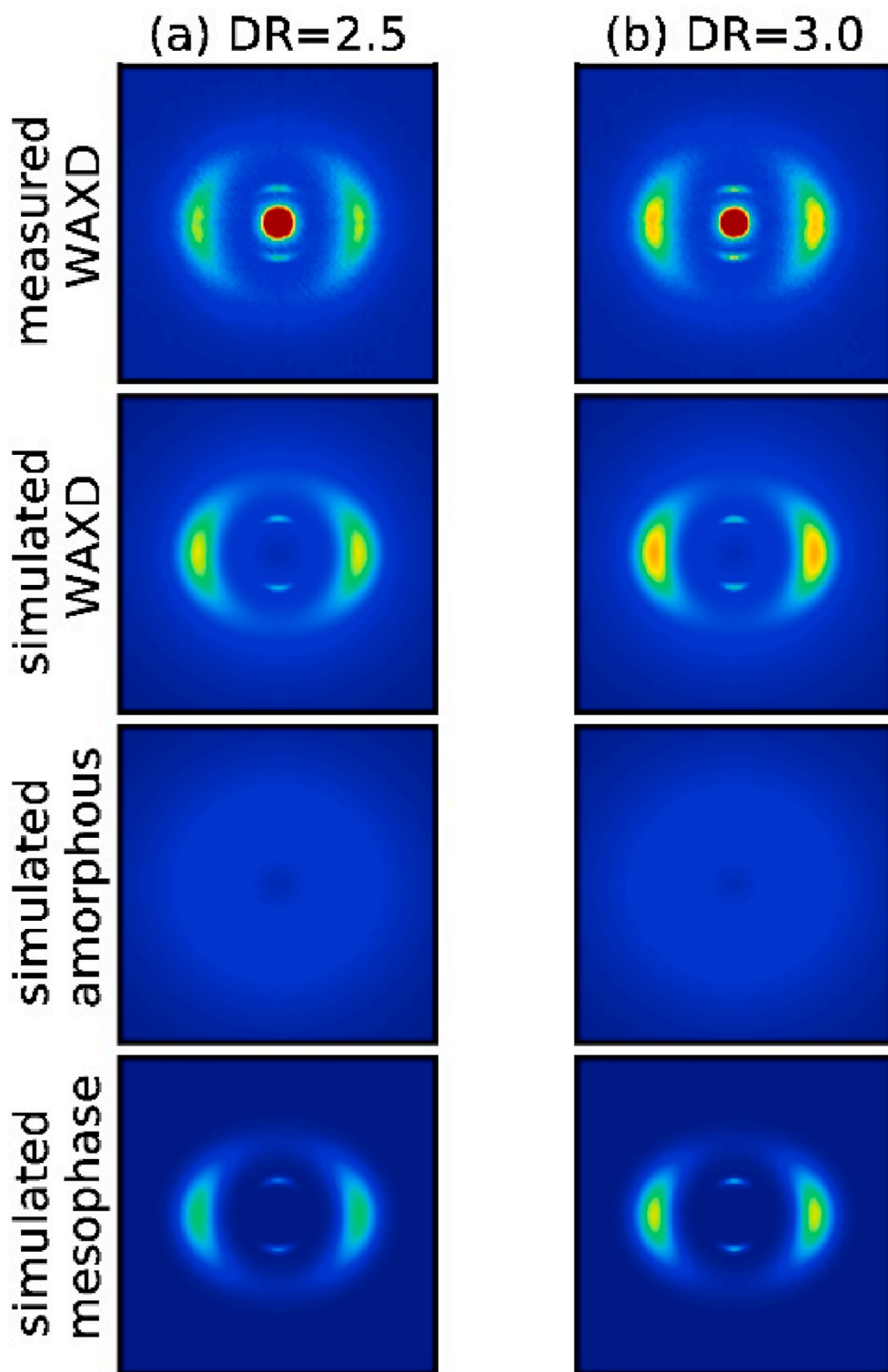


Fig. 6. Measured WAXD patterns of coPA fibers for different draw ratios (1st row), simulated WAXD patterns resulting from the fits (2nd row), simulated amorphous phase (3rd row) and simulated mesophase (4th row).

WAXD patterns of two coPA fibers of draw ratios 2.5 and 3. Fitted profiles are shown in the data in brief [76].

Two broad equatorial peaks and two meridional reflections are observed. Similar WAXD patterns have been previously observed and discussed for PA6 and PA11 [39,99,100]. Such patterns with two broad equatorial reflections and two meridional reflections can in principle be explained by one of the following two models, i.e., a smectic mesophase,

where heavy amide groups in oriented macromolecules are aligned in planes perpendicular to the fiber axis, or a nematic mesophase, where the heavy amide groups have no, or only very little, lateral positional correlations, see also Fig. 1. In the literature, the former model is sometimes referred to as the ‘smectic β -phase’. Note that for smectic phases, also higher order reflections should be observed on the meridian. Additionally, for smectic phases, the meridional reflections are

Table 3

Best fit parameters for meridional reflection in WAXD patterns of coPA monofilaments.

CoPA fibers DR	P _{nc} mesophase, meridional reflection				
	E _{mer} ^{norm}	μ _{mer} ^{Pnc} (°)	d _{mer} ^{Pnc} (Å)	σ _{mer} (°)	ΔX _{mer} (Å)
2.5	1.27	8.1	10.9	0.5	8.95
3.0	1.48	8.0	11.1	0.5	10.0

typically very sharp along the meridian and also perpendicular to it, due to the long-range order along the fiber axis, and the medium-range order in lateral direction [23,38,101]. We had to add an additional decaying Gaussian peak to the fitting procedure in order to account for the meridional reflection in coPA. The fitting results of the meridional reflections are summarized in Table 3. Nematic and smectic phases can be distinguished by analyzing the full width at half maximum (FWHM) of the meridional reflection along the layer line (parallel to equator). In case of coPA, the FWHM decreases from 0.32 Å⁻¹ to 0.29 Å⁻¹ upon drawing and is calculated from the exponential decay function (Equation (4)), which is based on the decay parameter, ΔX_{mer}. The correlation lengths of the coPA chains, in lateral direction, is therefore increasing from about 3.1 Å to 3.5 Å upon drawing. The small values of the correlation lengths suggest that the scattering is a result of parallel, yet uncorrelated polymer chains (nematic). The fact that the meridional reflections are arc-shaped, and that no higher order reflections are observed, supports this finding. The equatorial mesophase position of 18.4° corresponds to a lateral chain spacing of 4.8 Å, which is the same spacing as the previously reported one for the β-form phase in PA6 [99]. The angular position of the meridional reflection in coPA correlates with a spacing along the fiber axis of about 11 Å, which is significantly larger than the reported distance (8.35 Å) between amide groups in PA6 fibers [99,102], but it is quite close to the distance (12.9 Å) reported for the pseudo-hexagonal phase in PA11 [100]. The C=O groups in the coPA are separated by 10 CH₂ groups, which is similar to the spacing in PA11 (10 CH₂ groups and an N-H group). Thus, the meridional reflection, observed for coPA, arises most-likely from the spacing with 10 CH₂ groups. The second spacer between amide groups, 4'-methylenebis (2-methylcyclohexanamine), seems not to be oriented along the fiber axis, but may be tilted away from it, since no additional meridional reflection is observed.

3.1.2.4. Summary of fitting parameters from PC, COP and coPA fibers.

The best fit parameters from PC, COP and coPA fibers are summarized in Table 4.

The angular position of the mesophase is directly correlated to lateral spacings between molecular chains through Bragg's law [103]. The positions of the Gaussian rings (isotropic scattering) of the amorphous phase are correlated with either the real space distances between chains (intermolecular interferences) or may reflect the distances between heavier atoms on individual chains (intramolecular interferences). The positions and calculated lateral spacings of the mesophase, and real space distances of the amorphous scattering contributions PC, COP and coPA fibers, are summarized in Table 5. Note that for the PC fibers with DR = 2 and DR = 3, a large part of the amorphous scattering (isotropic ring) that is located at 17.3° for DR = 1, becomes oriented and is converted to the mesophase. The remaining amorphous scattering signal is composed of contributions at small and high scattering angles. The fitted positions (given in brackets in Table 5) reflect, where the main part of the remaining amorphous signal is located, suggesting that chains with either small or larger lateral spacing may not be orientable. Note that for the other samples, COP and coPA, the amorphous ring positions are located much closer to the P_{nc} phase and thus, in these cases, the amorphous ring positions reflect the preferred lateral spacing in the amorphous phase.

Table 4
Phase percentages and best fit parameters for all WAXD patterns of fibers melt-drawn from amorphous materials.

DR	P _{nc} mesophase					Amorphous phase											
	$\chi_{\text{Pnc}}(\%)$	D_{norm}^a	$\mu_{\text{Pnc}}^{\text{max}}(^{\circ})$	$\sigma_{\text{Pnc}}(^{\circ})$	ΔX_{Pnc}	a	$\chi_{\text{amorph}}(\%)$	A_{norm}^a	B_{norm}^a	C_{norm}^a	$\mu_1(^{\circ})$	$\mu_2(^{\circ})$	$\mu_3(^{\circ})$	$\sigma_1(^{\circ})$	$\sigma_2(^{\circ})$	$\sigma_3(^{\circ})$	k
PC	1.0	0	–	–	–	–	100	3.33	–	2.31	17.3	–	18.6	2.2	–	9.1	1.00
	2.0	31.3	2.28	2.4	1.6	0.3	68.7	0.62	0.22	0.65	8.0	21.1	24.1	4.1	1.4	6.6	1.08
	3.0	31.4	2.27	2.4	1.7	0.4	68.6	0.58	0.24	0.63	8.5	21.0	24.2	3.8	1.3	6.6	1.08
COP	1.5	36.7	0.90	3.0	1.2	1.0	63.3	0.65	1.05	–	17.0	16.3	–	3.6	1.1	–	1.05
	2.0	38.2	0.98	3.0	1.4	1.2	61.8	0.59	0.97	–	17.1	16.3	–	3.8	1.1	–	1.07
	2.5	38.2	1.06	3.0	1.7	1.0	61.8	0.49	1.06	–	17.0	16.3	–	3.7	1.1	–	1.07
3.0	38.0	1.13	3.0	1.9	0.7	62.0	0.43	1.14	–	17.1	16.3	–	3.9	1.1	–	1.08	
coPA	2.5	32.0	2.19	2.7	2.1	0.0	68.0	0.58	–	–	15.4	–	–	12.2	–	–	1.11
	3.0	33.3	2.28	2.7	2.3	0.1	66.7	0.49	–	–	15.2	–	–	13.0	–	–	1.15

^a All peak heights have been normalized to the peak height in the equatorial profile.

^a All peak heights have been normalized to the peak height in the equatorial profile.

Table 5

Scattering feature positions and calculated lateral spacings and real space distances. The explanation of values in brackets is given in the main text.

	DR	P _{nc} mesophase		Amorphous phase					
		$\mu_{\text{Pnc}}^{\text{max}}(^{\circ})$	$d_{\text{Pnc}}(\text{\AA})$	$\mu_1(^{\circ})$	$d_1(\text{\AA})$	$\mu_2(^{\circ})$	$d_2(\text{\AA})$	$\mu_3(^{\circ})$	$d_3(\text{\AA})$
PC	1.0	–	–	17.3	5.1	–	–	18.6	4.8
	2.0	17.1	5.2	(8.0)	(11.0)	(21.1)	(4.2)	(24.1)	(3.7)
	3.0	17.1	5.2	(8.5)	(10.4)	(21.0)	(4.2)	(24.2)	(3.7)
COP	1.5	16.8	5.3	17.0	5.2	16.3	5.4	–	–
	2.0	16.7	5.3	17.1	5.2	16.3	5.4	–	–
	2.5	17.1	5.2	17.0	5.2	16.3	5.4	–	–
	3.0	17.1	5.2	17.1	5.2	16.3	5.4	–	–
coPA	2.5	18.4	4.8	15.4	5.7	–	–	–	–
	3.0	18.4	4.8	15.2	5.8	–	–	–	–

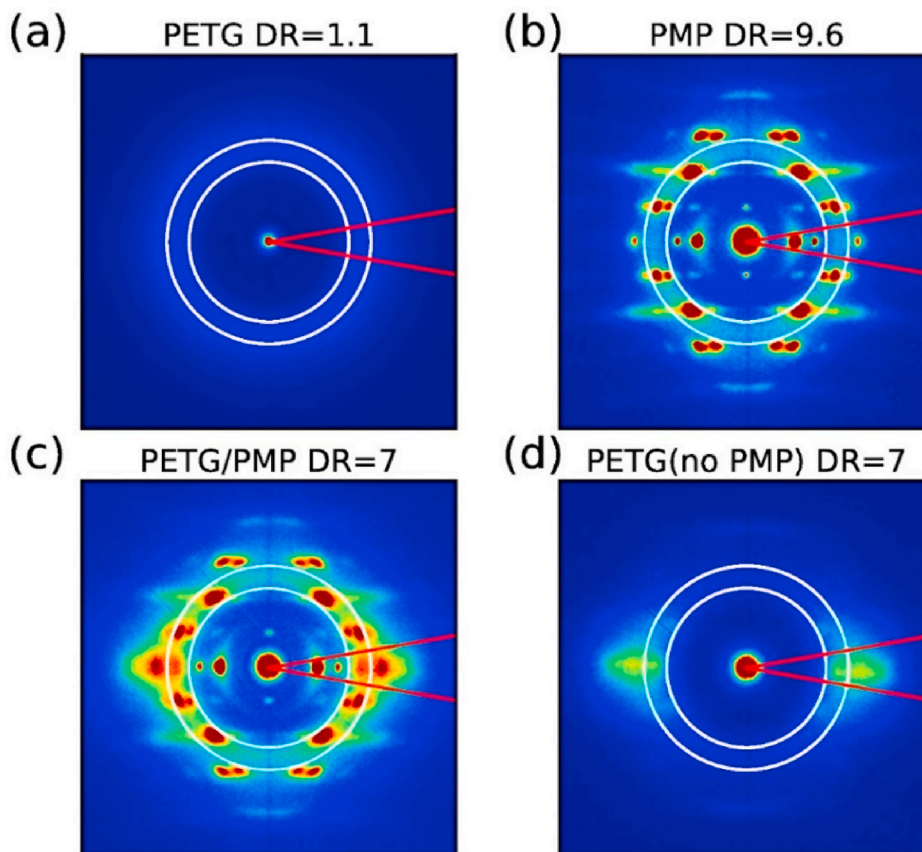


Fig. 7. Measured WAXD patterns of (a) PETG monofilament, (b) PMP monofilament, (c) PETG/PMP bicomponent fiber, (d) PETG core of bicomponent fiber with removed sheath. The integrated equatorial and azimuthal areas for the profile extractions are indicated with red lines and white circles. The profiles are shown in the data in brief [76]. (For interpretation of the references to colour in this figure legend, the reader is referred to the Web version of this article.)

3.1.2.5. PETG/PMP bicomponent monofilament. PETG is a random copolymer that consists of ethylene glycol terephthalate (ET) and 1,4-cyclohexanedimethanol terephthalate (CT) units (Table 2). A WAXD pattern of a PETG monofilament with DR = 1.1 is shown in Fig. 7a. PETG fibers can typically only be post-drawn with small DRs (<2), since the solidified fibers would break at high strain, due to lacking draw strength [41]. The maximum draw ratio that we have achieved for PETG was 1.3. In contrast, the semi-crystalline material PMP (Fig. 7b) can be melt-spun and drawn to very high draw ratios (here, DR = 9.6, see Fig. 7b). Various polymorphs of the PMP crystal structure are known [104–110]. Note that determining the exact crystal structure present in the PMP monofilament would exceed the scope of this article. Interestingly, it was possible to melt-spin PETG/PMP bicomponent fibers with a high draw ratio of 7.0 (Fig. 7c), since the sheath material provided the required draw strength. In bicomponent spinning, drawing stress is concentrated

in the polymer that solidifies first [111], i.e., in the semi-crystalline PMP. Since the PMP sheath has a lower glass transition temperature ($T_g = 20^{\circ}\text{C}$) [112] than the one of PETG ($T_g = 81^{\circ}\text{C}$ [113]), the PMP sheath is expected to thermally isolate the PETG core during melt-spinning, and therefore, to delay the freezing of molecular chain movement in PETG [111].

In order to measure the structure of the PETG core, we have removed the sheath from the bicomponent fiber by dissolving PMP in cyclohexane. The WAXD pattern of the resulting PETG core fiber, as shown in Fig. 7d, displays a strong mesophase that looks very similar to the one of PET [12].

Extracted equatorial profiles and azimuthal profiles highlight the existence of the mesophase in the PETG core material [76], verifying that the PETG core material had more time to orient itself due to the delayed cooling.

We conclude that amorphous materials can reach much higher draw ratios, when surrounded by a sheath material that has a lower glass transition temperature than the core. In the past, a similar behavior has been observed for PET/polystyrene [111,114] and for PET/polymethylmethacrylat [115] as well as for PET/PA6 [116] bicomponent filaments.

3.2. Drawn fibers melt-spun from semi-crystalline polymers

We have already applied the here presented WAXD fitting algorithms, for phases occurring in a semi-crystalline material, to melt-spun poly(ϵ -caprolactone) (PCL) [92]. In the following sections, we discuss the application of the algorithms to PET and P3HB filaments.

3.2.1. Uniqueness of fitting algorithm

Other methods exist to extract the mesophase content from WAXD patterns [8,47,49,63,72,74]. Most of the publications extract the isotropic fraction (amorphous) from the WAXD pattern with the ‘halo’ method, or from meridional profiles. Typically, the found isotropic fraction is then subtracted from the data, and the remaining anisotropic scattering that consists of crystalline phase and mesophase are fitted to specific functions. The here proposed algorithm is deconvolving mesophase and crystalline phase in a new and unique way, and also fits the amorphous phase. Applying the ‘halo’ method to semi-crystalline materials can become problematic when i) the unoriented crystalline scattering features (sharp rings) overlap with the unoriented amorphous scattering feature (halo) or ii) the mesophase scattering signal smears out and even contributes to the meridional region. Therefore, we decided to obtain the amorphous phase contribution by simultaneously fitting various profiles, i.e., equatorial, meridional, or off-axis and azimuthal profiles. For the crystalline fraction, the newly proposed algorithm takes into account atom types, atom positions and unit cell sizes, and calculates the structure factors from it. Furthermore, an oriented and unoriented crystalline fraction is taken into account. Thus, the

uniqueness of the proposed algorithms lies in the simultaneously obtained detailed information about amorphous phase, mesophase, as well as crystalline structure.

3.2.2. Poly(ethylene terephthalate) monofilament

Molecular structure and phases developing in PET have been widely studied in the past. We have therefore chosen to use PET as a fitting example in order to highlight the possibilities to simultaneously extract information about all the phases present in melt-spun fibers. The triclinic unit cell lattice parameters of PET from Daubeny et al. [95] ($a = 4.56 \text{ \AA}$, $b = 5.94 \text{ \AA}$, $c = 10.75 \text{ \AA}$) have slightly been adjusted, so that the simulated equatorial peak positions match the measured peak positions. The lattice parameters applied for the fits were: $a = 4.50 \text{ \AA}$, $b = 5.86 \text{ \AA}$ and $c = 10.75 \text{ \AA}$. The unit cell angles ($\alpha = 98.5^\circ$, $\beta = 118^\circ$, $\gamma = 112^\circ$) were adopted from Daubeny et al. [95]. Fractional coordinates (u, v, w) were taken from the refined values published by Tse et al. [96]. To calculate the orthogonal coordinates in angstrom, (r_x, r_y, r_z), from fractional coordinates of the triclinic unit cell, we have used Equations (11) and (12).

$$\begin{bmatrix} r_x \\ r_y \\ r_z \end{bmatrix} = \begin{bmatrix} a \sin \beta & \frac{b(\cos \gamma - \cos \alpha \cos \beta)}{\sin \beta} & 0 \\ 0 & \frac{\Omega}{ca \sin \beta} & 0 \\ a \cos \beta & b \cos \alpha & c \end{bmatrix} \begin{bmatrix} u \\ v \\ w \end{bmatrix} \quad (\text{Eq. 11})$$

$$\Omega = abc \sqrt{1 - \cos^2(\alpha) - \cos^2(\beta) - \cos^2(\gamma) + 2 \cos \alpha \cos \beta \cos \gamma} \quad (\text{Eq. 12})$$

A schematic of the triclinic unit cell in the orthogonal coordinate system is shown in Fig. 8a. Daubeny et al. [95] have found that the fiber axis has to be tilted with respect to the unit cell and have suggested that the fiber axis lies in the $(\bar{2}30)$ plane with a tilt angle of 5° . However, the tilt direction of the fiber axis and the absolute tilt value can vary, depending on the melt-spinning conditions [117]. This tilt of the crystalline unit cell, with respect to the fiber axis, strongly affects the

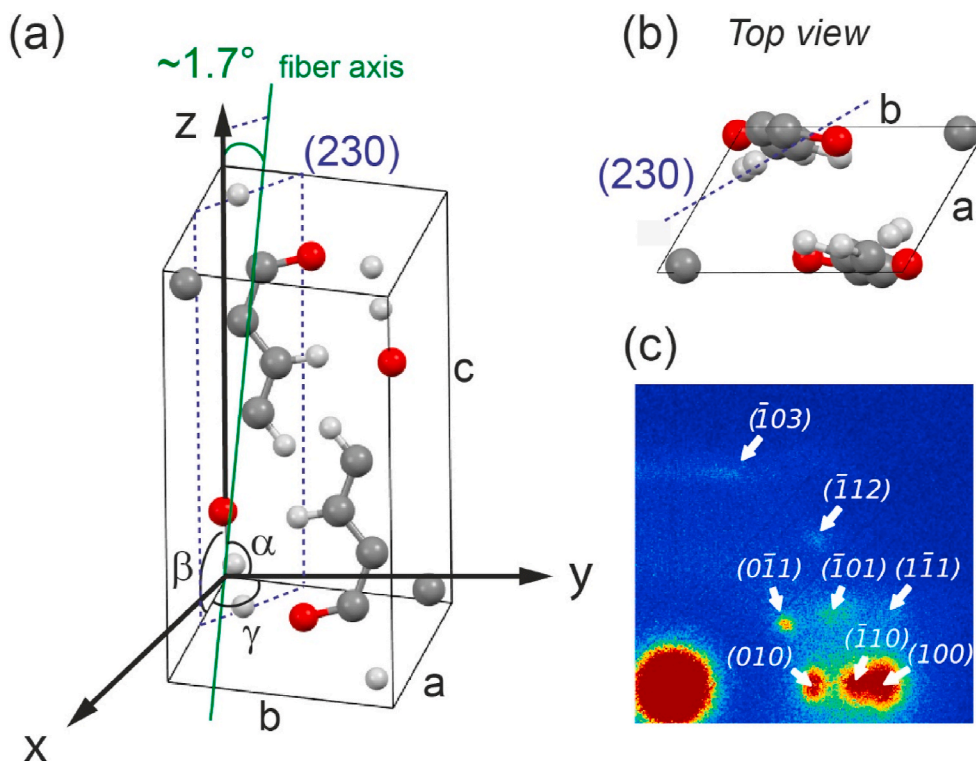


Fig. 8. (a) 3D view of triclinic unit cell of PET using the Mercury software [119]. Only bonds and atoms that fit entirely into the unit cell are shown. (b) Top view along the c-axis. (c) Corresponding reflections in the top-right quadrant of the WAXD pattern.

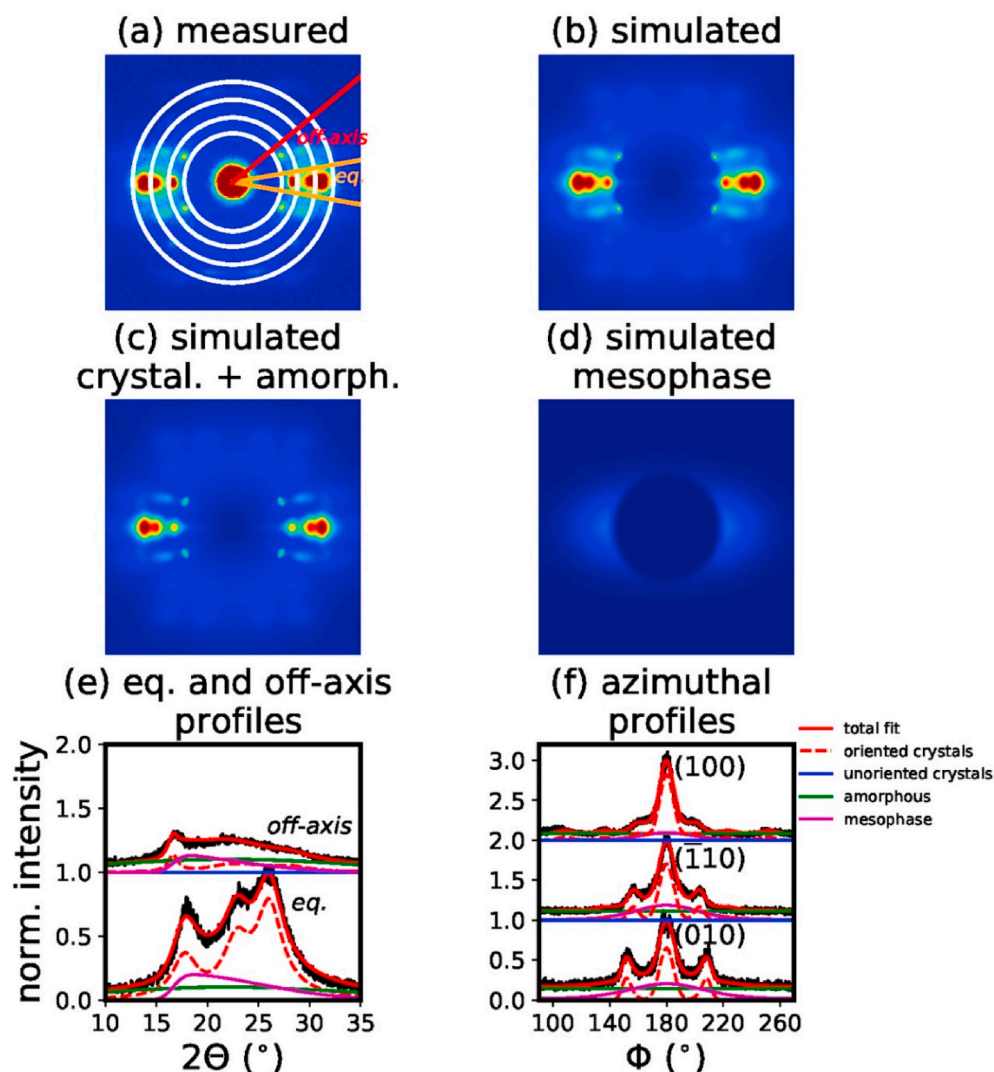


Fig. 9. (a) Measured WAXD pattern of PET fiber and (b) simulated pattern. (c) Simulated crystalline and amorphous contribution. (d) Mesophase contribution. (e) Corresponding fits of equatorial (eq.) and off-axis profiles. The integrated equatorial wedge lies between orange lines, and the off-axis wedge between the red and upper orange line, as shown in (a). The equatorial profiles and off-axis profiles are shown normalized to the maximum equatorial intensity. (f) Azimuthal profiles are normalized to the maximum azimuthal intensities. The off-axis and azimuthal profiles are offset by +1 for better visibility. (For interpretation of the references to colour in this figure legend, the reader is referred to the Web version of this article.)

Table 6
Phase percentages and relevant best fit parameters for the mesophase and crystalline phase in PET monofilaments.

P _{nc} mesophase							Crystalline phase							
χ _{Pnc} (%)	D _{norm}	μ _{Pnc} ^{max} (°)	d _{Pnc} (Å)	σ _{Pnc} (°)	ΔX _{Pnc}	a	χ _{crys} (%)	p	p ₀	x	W ₍₀₁₀₎ (nm)	W ₍₋₁₁₀₎ (nm)	W ₍₁₀₀₎ (nm)	W ₍₀₋₁₁₎ (nm)
16.3	0.29	18.7	4.7	7.7	2.1	9.08	27.0	142	0.0	0.009	2.1	1.9	2.0	5.8

diffraction patterns by shifting the reflections away from the layer line positions, either up- or downwards [95]. Considering the positions of the measured PET reflections, the fiber axis direction was found to lie in the (230) plane with a fiber direction vector of $\mathbf{f} = [-xa/2, xb/3, 1]$. All coordinates $[r_x, r_y, r_z]$ have thus been rotated [118] with a rotation matrix $\mathbf{R}(\mathbf{f}, t)$, which rotates the unit vector $\mathbf{f}/|\mathbf{f}|$ into the unit vector, $\mathbf{t} = \mathbf{R}(\mathbf{f}, t)\mathbf{f}$, with the tilt angle being defined through the fit parameter x . Such a fit, which enforced the tilt direction to be in the (230) plane, revealed a tilt angle of about 1.7° ($x = 0.009$) with the molecular axis being along $\mathbf{t} = [0, 0, 1]$ (see Fig. 8a and b). Fig. 8c shows the top-right quadrant of the measured WAXD pattern of a PET fiber, where (hkl) reflections are indicated with respect to the planes in the triclinic unit cell.

The entire WAXD pattern of the PET fiber is shown in Fig. 9a. Equatorial, off-axis and azimuthal profiles have been fitted, with the constraint that the tilt direction of the fiber axis has to lie in the (230) plane. The simulated WAXD pattern from the best fit parameters of all

phases is shown in Fig. 9b. The contribution to the 2D pattern, from the sum of crystalline and amorphous phase, is shown in Fig. 9c. The mesophase is asymmetric (Fig. 9d); the shape is very similar to the mesophases found in PET films [12], and the simulated data fits the extracted profiles remarkably well (Fig. 9e and f). Phase percentages and relevant best fit parameters, for the mesophase and crystalline phase, are summarized in Table 6. Additional parameters are given in the data in brief [76].

The mesophase scattering feature of PET is much broader than the ones found in stretched amorphous materials and is also more asymmetric. This suggests that there is a larger spread of lateral chain spacings between mesomorphic chains in PET, which could mean that the mesophase is on the verge of becoming crystalline. The decay of the mesophase away from the equator ($\Delta X_{Pnc} = 2.1$) is similar to the ones observed for the mesophase in amorphous materials (1.2–2.3), and thus, the mesophase is most-likely developing from the amorphous phase. In

the past, the mesophase has been said to be nematic or smectic-A [20, 32]. Since we observe no meridional reflections, we claim that the mesophase in the measured PET fiber has no lateral order, and is thus nematic.

The crystalline phase is highly oriented, which is reflected by the rather large p value, which corresponds to a Hermans' orientation parameter of 0.98 [98]. The crystal dimensions, $W_{(hkl)}$, in the direction perpendicular to the planes, are directly calculated from the width parameters of the respective reflections, and are also summarized in Table 6.

The crystal width values are a bit smaller than published parameters for crystals in PET films [120], which may be due to the neglected instrumental broadening. The crystals are found to be rather small in the a and b direction, but larger in the c direction.

3.2.3. Poly-3-hydroxybutyrate monofilaments

In previous articles, we have already discussed the mesophase in melt-spun P3HB filaments [4,5,83]. An as-spun P3HB fiber was stretched to different elongations, by applying different tensile stresses, which resulted in an increase of the mesophase and a concomitant decrease of crystalline α -phase. This transformation was found to be highly reversible [5]. Here, we have fitted the WAXD patterns of three

fiber samples: as-spun (0 N), elongated fiber with an applied force of 0.80 N (128 MPa) and 1.05 N (168 MPa), respectively. We have calculated the 2D WAXD pattern of the crystalline α -phase from the atomic coordinates and unit cell parameters ($a = 5.73$ Å, $b = 13.15$ Å and c (fiber axis) = 5.93 Å) previously published by Wang et al. [97]. To properly fit the data, we had to slightly extend the c -parameter to 6.02 Å for the as-spun fiber. Upon stretching, the a, b unit cell parameters needed also to be slightly decreased, and the c -parameter had to be increased [76]. For the fits, we have chosen to fit a profile of an off-axis wedge, the equatorial profile and also three azimuthal profiles. The latter profiles were extracted from integrated rings through the (020), (110) and mesophase reflections. Fitted profiles are shown in the data in brief [76], and the simulated 2D patterns are shown in Fig. 10. Note that the measured angular range was smaller for the P3HB fiber samples, compared to the angular ranges of other polymer fibers, since a longer sample to detector distance (16.8 cm) was used to fit the tensile stage into the diffractometer's vacuum chamber.

The most important fitting parameters, for the mesophase and crystalline phase, are summarized in Table 7. Additional parameters of, e.g., the amorphous phase, are given in the data in brief [76]. The phase percentage of the mesophase is increasing upon drawing, with a correlated decrease in the crystalline phase, which confirms our previous

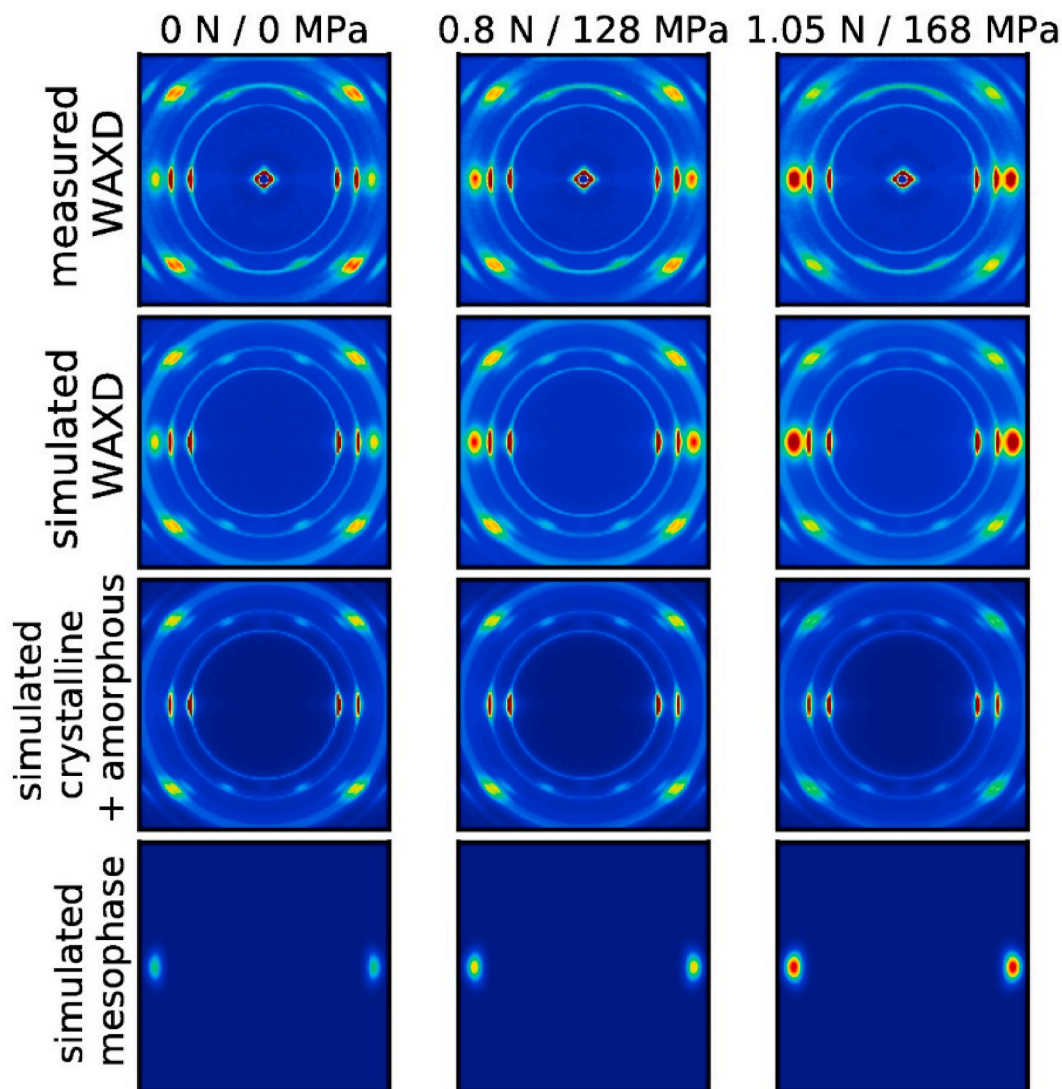


Fig. 10. Measured WAXD patterns of P3HB fiber (DR = 6) for different amounts of applied stress (1st row), simulated WAXD patterns resulting from the fits (2nd row), the sum of simulated crystalline and amorphous phase (3rd row), and simulated mesophase (4th row).

Table 7

Phase percentages and relevant best fit parameters for the mesophase and crystalline phase in P3HB monofilaments.

P3HB fibers (stress)	P _{nc} mesophase						Crystalline phase					
	$\chi_{\text{Pnc}}(\%)$	D_{norm}	$\mu_{\text{Pnc}}^{\text{max}}(^{\circ})$	$\sigma_{\text{Pnc}}(^{\circ})$	$\Delta\chi_{\text{Pnc}}$	a	$\chi_{\text{crys}}(\%)$	p	p ₀	$W_{(020)}$ (nm)	$W_{(110)}$ (nm)	k_{crys}
0 MPa	3.8	0.9	19.5	0.8	10.0	0.50	57.0	112	0.4	11.7	11.0	1.00
128 MPa	5.6	1.2	19.5	0.9	10.0	0.46	56.7	106	0.4	9.7	9.8	1.02
168 MPa	8.6	2.1	19.5	1.0	10.0	0.39	51.0	97	0.4	8.5	9.1	1.03

observations [5]. With the fitting procedure presented here, it is possible to simultaneously obtain information about the mesophase structure, as well as details about the crystalline and amorphous phase. The mesophase location, $\mu_{\text{Pnc}}^{\text{max}}$, corresponds to an average lateral spacing of the elongated chains of $d_{\text{Pnc}} = 4.6$ Å. The angular width, $\sigma_{\text{Pnc}} \sim 1^{\circ}$, of the mesophase peak, is reflecting the distribution of the various distances between the chains, and is smaller than the widths observed for the mesophases of the other materials described in this article (2.4 – 8°). This suggests, that the P3HB chains have a well-defined lateral spacing. From the width parameters of the reflections (020) and (110), one can directly calculate the crystal sizes, $W_{(020)}$ and $W_{(110)}$, along these crystalline directions (Table 7). A clear trend can be observed, i.e., the crystallinity is reducing and the crystal sizes are becoming smaller upon drawing, suggesting that the surface region (a few unit cells wide envelope) of highly-oriented α -crystals transforms into the mesophase, which confirms our previous findings [4,5]. Comparing the mesophase signal in drawn amorphous polymer materials with the mesophase signal in P3HB, it is obvious that the mesophase reflection in P3HB shows a much higher orientation. This is reflected by the large decay value of $\Delta\chi_{\text{Pnc}} \sim 10$, as opposed to the values of about 2, or smaller, in drawn amorphous fibers. This finding, and the previously observed reversibility behavior, support our hypothesis that the elongated chains of the P3HB mesophase most-likely consist of tie-molecules, which are located in-between oriented α -crystals. For P3HB films, it has been suggested that the width of the equatorial mesophase peak is correlated with the small crystal width of a hexagonal crystalline β -phase [121]. However, we did not observe any additional off-axis streaks or reflections that would confirm the existence of such a crystalline β -phase in our P3HB fibers.

The unoriented α -crystal fraction stays practically constant upon drawing, but follows an elliptic trace for the stretched samples, as is seen by the increase in the k_{crys} parameter [76]. The elliptic trace of unoriented crystals can be explained by the elongation of plane distances in the crystals along the fiber axis, and a concomitant compression of the crystals perpendicular to it.

4. Conclusions

In fiber development, one of the major tasks is to study the structure-property relationship in order to tailor fiber properties. Physical properties of polymer fibers strongly depend on the interplay between individual phases (amorphous, mesophase, crystalline) present in the fibers, as well as on molecular orientation and other structural properties [41]. Therefore, a detailed structural analysis, with e.g. wide angle x-ray diffraction, is essential to enhance fiber performance, to optimize melt-spinning processes and to ensure quality control.

In this article, we present a beneficial tool (2D WAXD fitting algorithms) to quantify all phases (amorphous, mesophase, crystalline) that are present in polymer fibers, melt-spun from either amorphous or semi-crystalline polymeric materials. With these fitting algorithms, it is possible to simultaneously obtain detailed structural information about chain spacings, molecular and crystalline orientations, as well as crystal sizes. The fitting procedure also leads to simulated 2D WAXD patterns, which is an ideal visualization of the fitting results. For the future, it is envisaged to convert the presented fitting algorithms into a Python GUI. The same algorithms have also the potential to be applied to extract

structural information of, e.g., stretched polymeric films.

We have shown that the applied drawing stress during melt-spinning can induce mesophases, not only in polymer fibers melt-drawn from semi-crystalline materials, but also in fibers produced from amorphous polymeric materials. The occurrence of mesophases in all fibers, analyzed in this work, lets us hypothesize that mesophases, where molecular chains align along the drawing axis, exist in all types of drawn polymer fibers, independent of the state of matter of the raw material (amorphous or semi-crystalline). The drawing is crucial for the development of mesophases, since the applied strain induces an orientation of the molecular chains, which in turn strongly affects the load-strain behavior of the fibers. The WAXD analysis has revealed that the mesophases have typically a limited amount of long-range order and are non-crystalline, meaning that no unit cell exists. Future molecular dynamics simulations on various polymeric materials under strain could provide new insights into mesophase formations.

Funding sources

Part of this work was funded by the Swiss Innovation Agency Innosuisse (project number: 26744.1).

Data availability

2D WAXD and SAXS data are available to download from <https://doi.org/10.17632/w73svj4xwr.1>.

CRediT authorship contribution statement

Edith Perret: Software, Formal analysis, Investigation, Data curation, Writing – original draft, Visualization. **Rudolf Hufenus:** Supervision, Project administration, Writing – review & editing.

Declaration of competing interest

The authors declare that they have no known competing financial interests or personal relationships that could have appeared to influence the work reported in this paper.

Acknowledgments

Authors would like to thank Benno Wüst for operating the melt-spinning plant and K. Jakubowski for helping with the removal of the PMP sheath. We also thank Burger et al. for providing us with basic Mathematica codes, which we have translated into Python, and have further developed for our fitting purposes. Additionally, we thank the people from the Center for X-ray Analytics (Empa, Dübendorf, Switzerland) for valuable discussions.

References

- [1] G. Friedel, Les états mésomorphes de la matière, *Ann. Phys.* 9 (18) (1922) 273–474.
- [2] J.K. Keum, H.J. Jeon, H.H. Song, J.I. Choi, Y.K. Son, Orientation-induced crystallization of poly(ethylene terephthalate) fibers with controlled microstructure, *Polymer* 49 (22) (2008) 4882–4888.

- [3] J.K. Keum, H.H. Song, Thermal deformations of oriented noncrystalline poly (ethylene terephthalate) fibers in the presence of mesophase structure, *Polymer* 46 (3) (2005) 939–945.
- [4] E. Perret, F.A. Reifler, A. Gooneie, K. Chen, F. Selli, R. Hufenus, Structural response of melt-spun poly(3-hydroxybutyrate) fibers to stress and temperature, *Polymer* 197 (2020) 122503.
- [5] E. Perret, F.A. Reifler, A. Gooneie, R. Hufenus, Tensile study of melt-spun poly(3-hydroxybutyrate) P3HB fibers: reversible transformation of a highly oriented phase, *Polymer* 180 (2019) 121668.
- [6] G. Wu, J.D. Jiang, P.A. Tucker, J.A. Cuculo, Oriented noncrystalline structure in PET fibers prepared with threadline modification process, *J. Polym. Sci. B Polym. Phys.* 34 (12) (1996) 2035–2047.
- [7] A.I. Abou-Kandil, G. Goldbeck-Wood, A.H. Windle, Molecular modeling of the intermediate smectic mesophase in polyethylene terephthalate, *Macromolecules* 40 (18) (2007) 6448–6453.
- [8] Y. Fu, W.R. Busing, Y. Jin, K.A. Affholter, B. Wunderlich, Structure analysis of the noncrystalline material in poly(ethylene terephthalate) fibers, *Macromol. Chem. Phys.* 195 (2) (1994) 803–822.
- [9] Y.G. Fu, B. Annis, A. Boller, Y.M. Jin, B. Wunderlich, Analysis of structure and properties of poly(ethylene-terephthalate) fibers, *J. Polym. Sci. B Polym. Phys.* 32 (13) (1994) 2289–2306.
- [10] E.B. Gowd, C. Ramesh, M.S. Byrne, N.S. Murthy, J. Radhakrishnan, Effect of molecular orientation on the crystallization and melting behavior in poly (ethylene terephthalate), *Polymer* 45 (19) (2004) 6707–6712.
- [11] R. Jakeways, J.L. Klein, I.M. Ward, The existence of a mesophase in poly(ethylene naphthalate), *Polymer* 37 (16) (1996) 3761–3762.
- [12] S.F. Ran, Z.G. Wang, C. Burger, B. Chu, B.S. Hsiao, Mesophase as the precursor for strain-induced crystallization in amorphous poly(ethylene terephthalate) film, *Macromolecules* 35 (27) (2002) 10102–10107.
- [13] T. Asano, F.J. Baltá Calleja, A. Flores, M. Tanigaki, M.F. Mina, C. Sawatari, H. Itagaki, H. Takahashi, I. Hattai, Crystallization of oriented amorphous poly (ethylene terephthalate) as revealed by X-ray diffraction and microhardness, *Polymer* 40 (23) (1999) 6475–6484.
- [14] J. Menczel, B. Wunderlich, Heat capacity hysteresis of semicrystalline macromolecular glasses, *J. Polym. Sci., Polym. Lett. Ed.* 19 (5) (1981) 261–264.
- [15] J.D. Menczel, M. Jaffe, How did we find the rigid amorphous phase? *J. Therm. Anal. Calorim.* 89 (2) (2007) 357–362.
- [16] Y. Tian, J. Zhou, J. Feng, The effect of thermal history on crystalline structure and mechanical properties of β -nucleated isotactic polypropylene, *Mater. Res. Express* 5 (4) (2018), 045304.
- [17] J.Y. Chen, P.A. Tucker, J.A. Cuculo, High-performance PET fibers via liquid isothermal bath high-speed spinning: fiber properties and structure resulting from threadline modification and posttreatment, *J. Appl. Polym. Sci.* 66 (13) (1997) 2441–2455.
- [18] T. Asano, T. Seto, Morphological studies of cold drawn poly(ethylene terephthalate), *Polym. J.* 5 (1) (1973) 72–85.
- [19] F. Auriemma, C. De Rosa, P. Corradini, Solid mesophases in semicrystalline polymers: structural analysis by Diffraction Techniques, in: G. Allegra (Ed.), *Interphases and Mesophases in Polymer Crystallization II*, Springer Berlin Heidelberg, Berlin, Heidelberg, 2005, pp. 1–74.
- [20] A.I. Abou-Kandil, A.H. Windle, The development of microstructure in oriented polyethylene terephthalate (PET) during annealing, *Polymer* 48 (17) (2007) 5069–5079.
- [21] D.J. Blundell, A. Mahendrasingam, C. Martin, W. Fuller, Formation and decay of a smectic mesophase during orientation of a PET/PEN copolymer, *J. Mater. Sci.* 35 (20) (2000) 5057–5063.
- [22] G. Farrow, Measurement of the smectic content in undrawn polypropylene filaments, *J. Appl. Polym. Sci.* 9 (4) (1965) 1227–1232.
- [23] G.E. Welsh, D.J. Blundell, A.H. Windle, A transient liquid crystalline phase as a precursor for crystallization in random Co-polyester fibers, *Macromolecules* 31 (21) (1998) 7562–7565.
- [24] G. GW, *Liquid Crystals and Plastic Crystals*, Wiley, Chichester, 1974.
- [25] S. N, *The Plastically Crystalline State (Orientationally Disordered Crystals)*, Wiley, Chichester, 1979.
- [26] R. Androsch, M.L. Di Lorenzo, C. Schick, B. Wunderlich, Mesophases in polyethylene, polypropylene, and poly(1-butene), *Polymer* 51 (21) (2010) 4639–4662.
- [27] Condis crystals and their relation to liquid crystals, in: B. Wunderlich, M. Möller, J. Grebowicz, H. Baur (Eds.), *Conformational Motion and Disorder in Low and High Molecular Mass Crystals*, Springer Berlin Heidelberg, Berlin, Heidelberg, 1988, pp. 67–95.
- [28] Condis crystals of flexible macromolecules, in: B. Wunderlich, M. Möller, J. Grebowicz, H. Baur (Eds.), *Conformational Motion and Disorder in Low and High Molecular Mass Crystals*, Springer Berlin Heidelberg, Berlin, Heidelberg, 1988, pp. 44–66.
- [29] Condis crystals of stiff macromolecules, in: B. Wunderlich, M. Möller, J. Grebowicz, H. Baur (Eds.), *Conformational Motion and Disorder in Low and High Molecular Mass Crystals*, Springer Berlin Heidelberg, Berlin, Heidelberg, 1988, pp. 96–103.
- [30] J. Grebowicz, S.F. Lau, B. Wunderlich, The thermal properties of polypropylene, *J. Polym. Sci., Polym. Symp.* 71 (1) (1984) 19–37.
- [31] B. Wunderlich, J. G, *Adv. Polym. Sci.* 60/61 (1984) 1.
- [32] F. Auriemma, P. Corradini, C. De Rosa, G. Guerra, V. Petraccone, R. Bianchi, G. Di Dino, On the mesomorphic form of poly(ethylene terephthalate), *Macromolecules* 25 (9) (1992) 2490–2497.
- [33] A.H. Windle, *Liquid Crystalline and Mesomorphic Polymers*, Springer, New York, 1994.
- [34] Z.-G. Wang, B.S. Hsiao, S. Srinivas, G.M. Brown, A.H. Tsou, S.Z.D. Cheng, R. S. Stein, Phase transformation in quenched mesomorphic isotactic polypropylene, *Polymer* 42 (18) (2001) 7561–7566.
- [35] R. Hosemann, A.M. Hindeleh, Structure of crystalline and paracrystalline condensed matter, *J. Macromol. Sci. Phys.* B34 (4) (1995) 327–356.
- [36] M. Barón, R.F.T. Stepto, Definitions of basic terms relating to polymer liquid crystals (IUPAC Recommendations 2001), *Pure Appl. Chem.* 74 (3) (2002) 493–509.
- [37] E. Pérez, M.L. Cerrada, A. García-Peñas, J.M. Gómez-Elvira, J.P. Fernández-Blázquez, A. Martínez-Gómez, D. López-Velázquez, J.C. Martínez, The role of mesophases in the ordering of polymers, *Eur. Polym. J.* 81 (2016) 661–673.
- [38] O.E. Piro, G.A. Echeverría, F.D. Cukiernik, Crystallography and the liquid crystal phase: a new approach to structural studies on a thermo-tropic smectic Schiff base, *Crystallogr. Rev.* 24 (1) (2018) 3–21.
- [39] J.-R. Xu, X.-K. Ren, T. Yang, X.-Q. Jiang, W.-Y. Chang, S. Yang, A. Stroeks, E.-Q. Chen, Revisiting the thermal transition of β -form polyamide-6: evolution of structure and morphology in uniaxially stretched films, *Macromolecules* 51 (1) (2018) 137–150.
- [40] F. Bedoui, N.S. Murthy, J. Kohn, Structure and thermal transitions in a biomedically relevant liquid crystalline poly(ester amide), *Macromolecules* 50 (6) (2017) 2257–2266.
- [41] R. Hufenus, Y. Yan, M. Dauner, T. Kikutani, Melt-spun fibers for textile applications, *Materials* 13 (19) (2020).
- [42] A.A. Leal, G. Mohanty, F.A. Reifler, J. Michler, R. Hufenus, Mechanical response of melt-spun amorphous filaments, *Sci. Technol. Adv. Mater.* 15 (3) (2014) 11.
- [43] N.S. Murthy, H. Minor, C. Bednarczyk, S. Krimm, Structure of the amorphous phase in oriented polymers, *Macromolecules* 26 (7) (1993) 1712–1721.
- [44] J.R. Katz, X-ray spectroscopy of polymers and in particular those having a rubber-like extensibility, *Trans. Faraday Soc.* 32 (1936) 77–94, 0.
- [45] S. Krimm, A.V. Tobolsky, Quantitative X-ray studies of order in amorphous and crystalline polymers - scattering from various polymers and a study of the glass transition in polystyrene and polymethyl methacrylate, *Textil. Res. J.* 21 (11) (1951) 805–822.
- [46] C. Wutz, D. Gieseler, T. Maevis, N. Stribeck, Molecular order of the mesogens in smectic poly(ester imide) fibers, *Macromolecules* 32 (14) (1999) 4658–4667.
- [47] S. Ran, X. Zong, D. Fang, B.S. Hsiao, B. Chu, R. Ross, Novel image analysis of two-dimensional X-ray fiber diffraction patterns: example of a polypropylene fiber drawing study, *J. Appl. Crystallogr.* 33 (4) (2000) 1031–1036.
- [48] Y. Mao, X. Li, C. Burger, B.S. Hsiao, A.H. Tsou, 2D WAXS/SAXS study on isotactic propylene-1-butylene random copolymer subjected to uniaxial stretching: the influence of temperature, *Polymer* 54 (4) (2013) 1432–1439.
- [49] B.L. Deopura, V. Kumar, T.B. Sinha, Melting behaviour and crystalline, intermediate and amorphous phase in poly(ethylene terephthalate) fibres, *Polymer* 18 (8) (1977) 856–857.
- [50] J.K. Keum, J. Kim, S.M. Lee, H.H. Song, Y.-K. Son, J.-I. Choi, S.S. Im, Crystallization and transient mesophase structure in cold-drawn PET fibers, *Macromolecules* 36 (26) (2003) 9873–9878.
- [51] Y. Liu, L. Yin, H. Zhao, G. Song, F. Tang, L. Wang, H. Shao, Y. Zhang, Lamellar and fibrillar structure evolution of poly(ethylene terephthalate) fiber in thermal annealing, *Polymer* 105 (2016) 157–166.
- [52] A. Mahendrasingam, C. Martin, W. Fuller, D.J. Blundell, R.J. Oldman, D. H. MacKerron, J.L. Harvie, C. Riekel, Observation of a transient structure prior to strain-induced crystallization in poly(ethylene terephthalate), *Polymer* 41 (3) (2000) 1217–1221.
- [53] N.S. Murthy, C. Bednarczyk, P.B. Rim, C.J. Nelson, Measurement of amorphous orientation in poly(ethylene terephthalate) fibers by X-ray diffraction and its significance, *J. Appl. Polym. Sci.* 64 (7) (1997) 1363–1371.
- [54] N.S. Murthy, S.T. Correale, H. Minor, Structure of the amorphous phase in crystallizable polymers - poly(ethylene terephthalate), *Macromolecules* 24 (5) (1991) 1185–1189.
- [55] E. Gorlier, J.M. Haudin, N. Billon, Strain-induced crystallisation in bulk amorphous PET under uni-axial loading, *Polymer* 42 (23) (2001) 9541–9549.
- [56] M.C. García Gutiérrez, J. Karger-Kocsis, C. Riekel, Cold drawing-induced mesophase in amorphous poly(ethylene naphthalate) revealed by X-ray microdiffraction, *Macromolecules* 35 (19) (2002) 7320–7325.
- [57] G. Stoclet, J.M. Lefebvre, B. Yeniad, G. Gobius du Sart, S. de Vos, On the strain-induced structural evolution of Poly(ethylene-2,5-furanoate) upon uniaxial stretching: an in-situ SAXS-WAXS study, *Polymer* 134 (2018) 227–241.
- [58] Y. Mao, D.G. Bucknall, R.M. Krieger, Synchrotron X-ray scattering study on amorphous poly(ethylene furanoate) under uniaxial deformation, *Polymer* 139 (2018) 60–67.
- [59] N.S. Murthy, R.G. Bray, S.T. Correale, R.A.F. Moore, Drawing and annealing of nylon-6 fibers - studies of crystal-growth, orientation of amorphous and crystalline domains and their influence on properties, *Polymer* 36 (20) (1995) 3863–3873.
- [60] N.S. Murthy, S.T. Correale, R.A.F. Moore, Characterization of the amorphous phase in nylon 6 fibers by x-ray diffraction, *J. Appl. Polym. Sci. Appl. Polym. Symp.* 47 (1991) 185–197.
- [61] A.H. Narten, A. Habenschuss, A. Xenopoulos, Diffraction pattern and structure of amorphous and crystalline regions in semicrystalline nylon 6.6, *Polymer* 32 (11) (1991) 1923–1927.
- [62] X. Xiao, Z. Cai, K. Qian, Structure evolution of polyamide (11)'s crystalline phase under uniaxial stretching and increasing temperature, *J. Polym. Res.* 24 (5) (2017) 81.

- [63] J. Wu, J.M. Schultz, Calculation of mesophase percentage of polymer fibers from 2D wide-angle X-ray scattering patterns, *Polymer* 43 (25) (2002) 6695–6700.
- [64] Z. Wang, C. Zhang, Z. Zhang, X. Chen, X. Wang, M. Wen, B. Chen, W. Cao, C. Liu, Polyethylene oxide enhances the ductility and toughness of polylactic acid: the role of mesophase, *Soft Matter* 16 (30) (2020) 7018–7032.
- [65] R. Lv, B. Na, N. Tian, S. Zou, Z. Li, S. Jiang, Mesophase formation and its thermal transition in the stretched glassy polylactide revealed by infrared spectroscopy, *Polymer* 52 (21) (2011) 4979–4984.
- [66] Q. Ma, M. Pyda, B. Mao, P. Cebe, Relationship between the rigid amorphous phase and mesophase in electrospun fibers, *Polymer* 54 (10) (2013) 2544–2554.
- [67] J.F. Mano, Structural evolution of the amorphous phase during crystallization of poly(l-lactic acid): a synchrotron wide-angle X-ray scattering study, *J. Non-Cryst. Solids* 353 (26) (2007) 2567–2572.
- [68] A. Morel, S. Domaschke, V. Urundilil Kumaran, D. Alexeev, A. Sadeghpour, S. N. Ramakrishna, S.J. Ferguson, R.M. Rossi, E. Mazza, A.E. Ehret, G. Fortunato, Correlating diameter, mechanical and structural properties of poly(l-lactide) fibres from needleless electrospinning, *Acta Biomater.* 81 (2018) 169–183.
- [69] G. Stoclet, R. Seguela, J.M. Lefebvre, C. Rochas, New insights on the strain-induced mesophase of poly(d,l-lactide): in situ WAXS and DSC study of the thermo-mechanical stability, *Macromolecules* 43 (17) (2010) 7228–7237.
- [70] J.-N. Wang, Y.-M. Zhang, X.-Y. Li, Effect of the draw ratio in dry jet-wet spinning on aromatic polysulfonamide fibers, *Nucl. Sci. Tech.* 31 (7) (2020) 63.
- [71] A.I. Abou-Kandil, A. Flores, F.J. Balta Calleja, A.H. Windle, Microindentation technique as a tool for investigating the development of order in PET under uniaxial stress, *J. Polym. Res.* 15 (5) (2008) 373–379.
- [72] T. Sun, A. Zhang, F.M. Li, R.S. Porter, Crystal lattice deformation and the mesophase in poly(ethylene terephthalate) uniaxially drawn by solid-state coextrusion, *Polymer* 29 (12) (1988) 2115–2120.
- [73] C. Zhang, Y. Zhang, J. Luo, J. Shi, H. Shao, X. Hu, Microstructural evolution of regenerated silk fibroin/graphene oxide hybrid fibers under tensile deformation, *RSC Adv.* 7 (6) (2017) 3108–3116.
- [74] G. Lemanska, A. Narebska, Quantitative determination of mesomorphic regions in oriented polymers from wide-angle X-ray diffraction, *J. Polym. Sci. Polym. Phys. Ed* 18 (5) (1980) 917–926.
- [75] R. Hufenus, F.A. Reifler, K. Maniura-Weber, A. Spierings, M. Zinn, Biodegradable bicomponent fibers from renewable sources: melt-spinning of poly(lactic acid) and poly[(3-hydroxybutyrate)-co-(3-hydroxyvalerate)], *Macromol. Mater. Eng.* 297 (1) (2012) 75–84.
- [76] E. Perret, R. Hufenus, Fitting of 2D WAXD data: mesophases in polymer fibers (under review), 2021. Data in Brief.
- [77] Datasheet for lexan 103R, Available from, <https://www.sabic.com/en/products>.
- [78] Datasheets for ZEONEX and ZEONOR cyclo olefin polymer (COP), Available from, <http://www.zeonex.com/datasheets.asp>.
- [79] F.A. Reifler, R. Hufenus, M. Krehel, E. Zraggen, R.M. Rossi, L.J. Scherer, Polymer optical fibers for textile applications - bicomponent melt spinning from cyclic olefin polymer and structural characteristics revealed by wide angle X-ray diffraction, *Polymer* 55 (22) (2014) 5695–5707.
- [80] Datasheet for Grilamid TR90, Available from, <https://www.emsgrivory.com/de/produkte-und-maerkte/produkte/grilamid/grilamid-tr/>.
- [81] T. Chen, J. Zhang, H. You, Photodegradation behavior and mechanism of poly(ethylene glycol-co-1,4-cyclohexanedimethanol terephthalate) (PETG) random copolymers: correlation with copolymer composition, *RSC Adv.* 6 (104) (2016) 102778–102790.
- [82] Datasheet for TPX™, Available from, <https://us.mitsuichemicals.com/service/product/tpx.htm>.
- [83] R. Hufenus, F.A. Reifler, M.P. Fernandez-Ronco, M. Heuberger, Molecular orientation in melt-spun poly(3-hydroxybutyrate) fibers: effect of additives, drawing and stress-annealing, *Eur. Polym. J.* 71 (2015) 12–26.
- [84] E. Perret, F.A. Reifler, A. Gooneie, K. Chen, F. Selli, R. Hufenus, X-ray data about the structural response of melt-spun poly(3-hydroxybutyrate) fibers to stress and temperature Data in, Brief 31 (2020) 105675.
- [85] E. Perret, F.A. Reifler, A. Gooneie, R. Hufenus, X-ray data from a cyclic tensile study of melt-spun poly(3-hydroxybutyrate) P3HB fibers: a reversible mesophase, Data in Brief 25 (2019) 104376.
- [86] K. Hareesh, A.K. Pandey, Y. Sangappa, R. Bhat, A. Venkataraman, G. Sanjeev, Changes in the properties of Lexan polycarbonate by UV irradiation, *Nucl. Instrum. Methods Phys. Res. Sect. B Beam Interact. Mater. Atoms* 295 (2013) 61–68.
- [87] K. Tulsyan, S. Toshniwal, G. Dorairaju, D.F. Schmidt, E. Reynaud, Thermomechanical assessment of plastic deformation in model amorphous polyamide/clay nanocomposites, *J. Nanomater.* 2010 (2010) 679786.
- [88] J. Kieffer, J.P. Wright, PyFAI: a Python library for high performance azimuthal integration on GPU, *Powder Diff.* 28 (S2) (2013) S339–S350.
- [89] C. Burger, B.S. Hsiao, B. Chu, Preferred orientation in polymer fiber scattering, *Polym. Rev.* 50 (1) (2010) 91–111.
- [90] Y. Mao, C. Burger, X. Li, B.S. Hsiao, A.K. Mehta, A.H. Tsou, Time-resolved synchrotron X-ray scattering study on propylene-1-butylene random copolymer subjected to uniaxial stretching at high temperatures, *Macromolecules* 45 (2) (2012) 951–961.
- [91] Y. Mao, C. Burger, F. Zuo, B.S. Hsiao, A. Mehta, C. Mitchell, A.H. Tsou, Wide-angle X-ray scattering study on shear-induced crystallization of propylene-1-butylene random copolymer: experiment and diffraction pattern simulation, *Macromolecules* 44 (3) (2011) 558–565.
- [92] F. Selli, U.H. Erdogan, R. Hufenus, E. Perret, Mesophase in melt-spun poly(ϵ -caprolactone) filaments: structure–mechanical property relationship, *Polymer* 206 (2020) 122870.
- [93] P.J. Brown, A.G. Fox, E.N. Maslen, M.A. O’Keefe, B.T.M. Willis, Intensity of diffracted intensities, in: E. Prince (Ed.), *International Tables for Crystallography Volume C: Mathematical, Physical and Chemical Tables*, Springer Netherlands, Dordrecht, 2004, pp. 554–595.
- [94] F. Selli, U.H. Erdogan, R. Hufenus, E. Perret, Properties, X-ray data and 2D WAXD fitting procedures of melt-spun poly(ϵ -caprolactone), Data in Brief 32 (2020) 106223.
- [95] R.D. Daubeny, C.W. Bunn, The crystal structure of polyethylene terephthalate, *Proc. Roy. Soc. Lond. Math. Phys. Sci.* 226 (1167) (1954) 531–542.
- [96] J.S. Tse, T.C.W. Mak, Refinement of the crystal structure of polyethylene terephthalate, *J. Cryst. Mol. Struct.* 5 (1975) 75–80.
- [97] H. Wang, K. Tashiro, Reinvestigation of crystal structure and intermolecular interactions of biodegradable poly(3-hydroxybutyrate) α -form and the prediction of its mechanical property, *Macromolecules* 49 (2) (2016) 581–594.
- [98] J.J. Hermans, P.H. Hermans, D. Vermaas, A. Weidinger, Quantitative evaluation of orientation in cellulose fibres from the X-ray fibre diagram, *Recueil Des Travaux Chim. Des Pays-Bas-J. Royal Netherlands Chem. Soc.* 65 (7–8) (1946) 427–447.
- [99] F. Auriemma, V. Petraccone, L. Parravicini, P. Corradini, Mesomorphic form (β) of nylon 6, *Macromolecules* 30 (24) (1997) 7554–7559.
- [100] J. Pepin, V. Gaucher, C. Rochas, J.-M. Lefebvre, In-situ SAXS/WAXS investigations of the mechanically-induced phase transitions in semi-crystalline polyamides, *Polymer* 175 (2019) 87–98.
- [101] G.E. Welsh, D.J. Blundell, A.H. Windle, A transient mesophase on drawing polymers based on polyethylene terephthalate (PET) and polyethylene naphthoate (PEN), *J. Mater. Sci.* 35 (20) (2000) 5225–5240.
- [102] Y. Li, W.A. Goddard, Nylon 6 crystal structures, folds, and lamellae from theory, *Macromolecules* 35 (22) (2002) 8440–8455.
- [103] W.H. Bragg, W.L. Bragg, The reflection of X-rays by crystals, *Proc. R. Soc. Lond. - Ser. A Contain. Pap. a Math. Phys. Character* 88 (605) (1913) 428–438.
- [104] I.W. Bassi, O. Bonsignori, G.P. Lorenzi, P. Pino, P. Corradini, P.A. Temussi, Structure and optical activity of a crystalline modification of isotactic poly-(S)-4-methyl-1-hexene, *J. Polym. Sci. 2 Polym. Phys.* 9 (2) (1971) 193–208.
- [105] C. De Rosa, Crystal structure of form II of isotactic poly(4-methyl-1-pentene), *Macromolecules* 36 (16) (2003) 6087–6094.
- [106] C. De Rosa, F. Auriemma, A. Borriello, P. Corradini, Up-down disorder in the crystal structure of form III of isotactic poly(4-methyl-1-pentene), *Polymer* 36 (25) (1995) 4723–4727.
- [107] C. De Rosa, A. Borriello, V. Venditto, P. Corradini, Crystal structure of form III and the polymorphism of isotactic poly(4-methylpentene-1), *Macromolecules* 27 (14) (1994) 3864–3868.
- [108] C. De Rosa, V. Venditto, G. Guerra, P. Corradini, Crystal structure of syndiotactic poly(4-methyl-1-pentene), *Polymer* 36 (19) (1995) 3619–3624.
- [109] F.C. Frank, A. Keller, A. O’Connor, Observations on single crystals of an isotactic polyolefin: morphology and chain packing in poly-4-methyl-pentene-1, *Phil. Mag.: A J. Theor. Exp. Appl. Phys.* 4 (38) (1959) 200–214.
- [110] H. Kusanagi, M. Takase, Y. Chatani, H. Tadokoro, Crystal structure of isotactic poly(4-methyl-1-pentene), *J. Polym. Sci. Polym. Phys. Ed* 16 (1) (1978) 131–142.
- [111] R. Hufenus, Y. Yan, M. Dauner, D. Yao, T. Kikutani, Bicomponent fibers, in: H. Jinlian, B. Kumar, J. Lu (Eds.), *Handbook of Fibrous Materials*, Wiley-VCH, Weinheim, Germany, 2018.
- [112] P. Zoller, The specific volume of poly(4-methylpentene-1) as a function of temperature (30°–320°C) and pressure (0–2000 kg/cm²), *J. Appl. Polym. Sci.* 21 (11) (1977) 3129–3137.
- [113] Datasheet for eastman eastar 6763, Available from, <https://www.eastman.com/Pages/ProductHome.aspx?product=71040786>.
- [114] T. Kikutani, S. Arikawa, A. Takaku, N. Okui, Fiber structure formation in high-speed melt spinning of sheath-core type bicomponent fibers, *Seni Gakkai Shi* 51 (9) (1995) 408–415.
- [115] M. Yoshimura, K. Iohara, H. Nagai, T. Takahashi, K. Koyama, Structure formation of blend and sheath/core conjugated fibers in high-speed spinning of PET, including a small amount of PMMA, *J. Macromol. Sci., Part B* 42 (2) (2003) 325–339.
- [116] E. Perret, O. Braun, K. Sharma, S. Tritsch, R. Muff, R. Hufenus, High-resolution 2D Raman mapping of mono- and bicomponent filament cross-sections, *Polymer* 229 (2021), 124011.
- [117] Y. Fu, W.R. Busing, Y. Jin, K.A. Affholter, B. Wunderlich, Poly(ethylene terephthalate) fibers. 1. Crystal structure and morphology studies with full-pattern x-ray diffraction refinement, *Macromolecules* 26 (9) (1993) 2187–2193.
- [118] T. Möller, J.F. Hughes, Efficiently building a matrix to rotate one vector to another, *J. Graph. Tool.* 4 (4) (1999) 1–4.
- [119] C.F. Macrae, I. Sovago, S.J. Cottrell, P.T.A. Galek, P. McCabe, E. Pidcock, M. Platings, G.P. Shields, J.S. Stevens, M. Towler, P.A. Wood, Mercury 4.0: from visualization to analysis, design and prediction, *J. Appl. Cryst.* 53 (2020).
- [120] D.R. Salem, Development of crystalline order during hot-drawing of poly(ethylene terephthalate) film: influence of strain rate, *Polymer* 33 (15) (1992) 3182–3188.
- [121] S. Phongsamrug, K. Tashiro, X-ray crystal structure analysis of poly(3-hydroxybutyrate) β -form and the proposition of a mechanism of the stress-induced α -to- β phase transition, *Macromolecules* 52 (8) (2019) 2995–3009.